An improved regional coupled modeling system for Arctic sea ice simulation and prediction: a case study for 2018

Chao-Yuan Yang[1], Jiping Liu[2], Dake Chen[1]

[1]School of Atmospheric Sciences, Sun Yat-sen University, and Southern Marine Science and Engineering Guangdong Laboratory (Zhuhai), Zhuhai, Guangdong, China

[2]Department of Atmospheric and Environmental Sciences, University at Albany, State University of New York, Albany, NY, USA

Corresponding authors:

Chao-Yuan Yang (yangchy36@mail.sysu.eu.cn) and Jiping Liu (jliu26@albany.edu)

Abstract

The improved/updated Coupled Arctic Prediction System (CAPS) is evaluated using a set of Pan-Arctic prediction experiments for the year 2018. CAPS is built on Weather Research and Forecasting model (WRF), the Regional Ocean Modeling System (ROMS), the Community Ice CodE (CICE), and a data assimilation based on the Local Error Subspace Transform Kalman Filter. We analyze physical processes linking improved/changed physical parameterizations in WRF, ROMS, and CICE to changes in the simulated Arctic sea ice state. Our results show that the improved convection and boundary layer schemes in WRF result in an improved simulation of downward radiative fluxes and near surface air temperature, which influences the predicted ice thickness. The changed tracer advection and vertical mixing schemes in ROMS reduce the bias in sea surface temperature and change ocean temperature and salinity structure in the surface layer, leading to improved evolution of the predicted ice extent (particularly correcting the late ice recovery issue in the previous CAPS). The improved sea ice thermodynamics in CICE have noticeable influences on the predicted ice thickness. The updated CAPS can better predict the evolution of Arctic sea ice during the melting season compared with its predecessor, though the prediction still has some biases at the regional scale. We further show that the updated CAPS can remain skillful beyond the melting season, which may have potential values for stakeholders to make decisions for socioeconomical activities in the Arctic.

1. Introduction

Over the past few decades, the extent of Arctic sea ice has decreased rapidly and entered a thinner/younger regime associated with global climate change (e.g., Kwok, 2018; Serreze and Meier, 2019). The dramatic changes in the properties of Arctic sea ice have gained increasing attentions by a wide range of stakeholders, such as trans-Arctic shipping, natural resource exploration, and activities of coastal communities relying on sea ice (e.g., Newton et al., 2016). This leads to increasing demands on skillful Arctic sea ice prediction, particularly at seasonal timescale (e.g., Jung et al., 2016; Liu et al., 2019; Stroeve et al., 2014). However, Arctic sea ice predictions based on different approaches (e.g., statistical method and dynamical model) submitted to the Sea Ice Outlook, a community effort managed by the Sea Ice Prediction Network (SIPN, https://www.arcus.org/sipn), show substantial biases in the predicted seasonal minimum of Arctic sea ice extent compared to the observations for most years since 2008 (Liu et al., 2019; Stroeve et al., 2014).

Recently, we have developed an atmosphere-ocean-sea ice regional coupled modeling system for seasonal Arctic sea ice prediction (Yang et al., 2020, hereafter Y20), in which the Community Ice CodE (CICE) is coupled with the Weather Research and Forecasting Model (WRF) and the Regional Ocean Modeling System (ROMS), hereafter called Coupled Arctic Prediction System (CAPS). To improve the accuracy of initial sea ice conditions, CAPS employs an ensemble-based data assimilation system to assimilate satellite-based sea ice observations. Seasonal Pan-Arctic sea ice predictions with improved initial sea ice conditions conducted in Y20 have shown that CAPS has the potential to provide skillful Arctic sea ice

prediction at seasonal timescale.

We know that the changes of sea ice variables (e.g., ice extent, ice concentration, ice thickness, ice drift) are mainly driven by forcings from the atmosphere and the ocean. Atmospheric cloudiness and related radiation influence surface ice melting (Huang et al., 2019; Kapsch et al., 2016; Kay et al., 2008) and the energy stored in the surface mixed layer that determines the seasonal ice melt and growth (e.g., Perovich et al., 2011, 2014). Atmospheric circulation is the primary driver for the transportation of sea ice and partly responsible for the variability of Arctic sea ice (e.g., Mallett et al., 2021; Ogi et al., 2010; Zhang et al., 2008). Olonscheck et al. (2019) suggested that atmospheric temperature fluctuations explain a majority of Arctic sea ice variability while other drivers (e.g., surface winds, and poleward heat transport) account for about 25% of Arctic sea ice variability. The oceanic heat inputs (as well as salt inputs) into the Arctic Ocean include the Atlantic Water (AW; Aagaard, 1989; McLaughlin et al., 2009) through the Barents Sea, and the Pacific Water (PW; Itoh et al., 2013; Woodgate et al., 2005) from the Bering Strait. The oceanic heat inputs from AW and PW are not directly available for sea ice since they are separated from a cold and fresh layer underlying sea ice (e.g., Carmack et al., 2015, Fig. 2). Vertical mixing by the internal wave (e.g., Fer, 2014) and double diffusion (e.g., Padman and Dillon, 1987; Turner, 1973) are the principal processes for upward heat transport from the subsurface layer (i.e., AW and PW) to the surface mixed layer in the Arctic Ocean. Sea ice thermodynamics determines how thermal properties of sea ice (e.g., temperature, salinity) change. These changes then influence the thermal structure of underlying ocean through interfacial fluxes (i.e., heat, salt and freshwater fluxes; DuVivier et

al., 2021; Kirkman IV and Bitz, 2011) and ice thickness (e.g., Bailey et al., 2020).

CAPS is configured for the Arctic with sufficient flexibility. That means each model component of CAPS (WRF, ROMS, and CICE) has different physics options for us to choose and capability to integrate ongoing improvements in physical parameterizations. Recently, the WRF model has adapted improved convection and boundary layer schemes in the Rapid Refresh (RAP) model operational at the National Centers for Environmental Prediction (NCEP, Benjamin et al., 2016). The first question we want to answer in this paper is to what extent these modifications can improve atmospheric simulations in the Arctic (i.e., radiation, temperature, humidity, and wind), and then benefit seasonal Arctic sea ice simulation and prediction. The ROMS model provides several options for tracer advection schemes. These advection schemes can have different degrees of oscillatory behavior (e.g., Shchepetkin and McWilliams, 1998). The oscillatory behavior can have impacts on sea ice simulation through ice-ocean interactions (e.g., Naughten et al., 2017). The second question we want to answer in this paper is to what extent different advection schemes can change the simulation of upper ocean thermal structure and then Arctic sea ice prediction. Several recent efforts have incorporated prognostic salinity into sea ice models. The CICE model has a new mushy-layer thermodynamics parameterization that includes prognostic salinity and treats sea ice as a two-phase mushy layer (Turner et al., 2013). Bailey et al. (2020) showed that the mushy-layer physics has noticeable impacts on Arctic sea ice simulation within the Community Earth System Model version 2. The third question we want to answer in this paper is whether the mushy-layer scheme can produce noticeable influence on seasonal Arctic sea ice prediction.

Currently, SIPN focuses on Arctic sea ice predictions during the melting season, particularly the seasonal minimum. It is not clear that how predictive skills of dynamical models participating in SIPN may change for longer period, i.e., extending into the freezing up period, which also have significance on socioeconomic aspects. The assessment of the skills of global climate models (GCMs) in predicting Pan-Arctic sea ice extent with suites of hindcasts suggested that GCMs may have skills at lead times of 1-6 months (e.g., Blanchard-Wrigglesworth et al., 2015; Chevallier et al., 2013; Guemas et al., 2016; Merryfield et al., 2013; Msadek et al., 2014; Peterson et al., 2015; Sigmond et al., 2013; Wang et al., 2013; Zampieri et al., 2018). Moreover, some studies using a "perfect model" approach, which treats one member of an ensemble as the truth (i.e., assuming the model is prefect without bias) and analyzes the skill of other members in predicting the response of the "truth" member (e.g., Meehl et al., 2007), suggested that Arctic sea ice cover can be potentially predictable up to two years in advance (e.g., Blanchard-Wrigglesworth et al., 2011; Blanchard-Wrigglesworth and Bushuk, 2018; Day et al., 2016; Germe et al., 2014; Tietsche et al., 2014). The last question we want to answer in this paper is whether CAPS has predictive skill for longer periods (up to 7 months).

This paper is structured as follows. Section 2 provides a brief overview of CAPS, including model configurations and data assimilation procedures. Section 3 describes the designs of the prediction experiments for the year of 2018 based on major improvements/ changes in the model components compared to its predecessor described in Y20, examines the performance of the updated CAPS, and offers physical links between Arctic sea ice changes

and improved/changed physical parameterizations. Section 4 discusses the predictive skill of CAPS at longer timescale. Discussions and concluding remarks are given in section 5.

2. Coupled Arctic Prediction System (CAPS)

As described in Y20, CAPS has been developed by coupling the Community Ice CodE (CICE) with the Weather Research and Forecasting Model (WRF) and the Regional Ocean Modeling System (ROMS) based on the framework of the Coupled Ocean-Atmosphere-Wave-Sediment Transport (Warner et al., 2010). The general description of each model component in CAPS is referred to Y20. The advantage of CAPS is its model components have a variety of physics for us to choose and capability to integrate follow-up improvements of physical parameterizations. With recent achievements of community efforts, we update CAPS based on newly-released WRF, ROMS, and CICE models. During this update, we focus on the Rapid Refresh (RAP) physics in the WRF model, the oceanic tracer advection scheme in the ROMS model, sea ice thermodynamics in the CICE model (see details in section 3), and investigate physical processes linking them to Arctic sea ice simulation and prediction. The same physical parameterizations described in Y20 are used here for the control simulation (see Table 1). Major changes in physical parameterizations as well as the model infrastructure in the WRF, ROMS, and CICE models are described in section 3.

As described in Y20, the Parallel Data Assimilation Framework (PDAF, Nerger and Hiller, 2013) was implemented in CAPS, which provides a variety of optimized ensemble-based Kalman filters. The Local Error Subspace Transform Kalman Filter (LESTKF; Nerger et al., 2012) is used to assimilate satellite-observed sea ice parameters. The LESTKF projects the

ensemble onto the error subspace and then directly computes the ensemble transformation in the error subspace. This results in better assimilation performance and higher computational efficiency compared to the other filters as discussed in Nerger et al. (2012).

The initial ensembles are generated by applying the second-order exact sampling (Pham, 2001) to simulated sea ice state vectors (ice concentration and thickness) from an one-month free run, and then assimilating sea ice observations, including: 1) the near real-time daily Arctic sea ice concentration processed by the National Aeronautics and Space Administration (NASA) Team algorithm (Maslanik and Stroeve, 1999) obtained from the NSIDC (https://nsidc.org/data/NSIDC-0081/), and 2) a combined monthly sea ice thickness derived from the CryoSat-2 (Laxon et al., 2013; obtained from http://data.seaiceportal.de), and daily sea ice thickness derived from the Soil Moisture and Ocean Salinity (SMOS; Kaleschke et al., 2012; Tian-Kunze et al., 2014; obtained from https://icdc.cen.uni-hamburg.de/en/l3c-smos-sit.html). To address the issue that sea ice thickness derived from CyroSat-2 and SMOS are unavailable during the melting season, the melting season ice thickness is estimated based on the seasonal cycle of the Pan-Arctic Ice Ocean Modeling and Assimilation System (PIOMAS) daily sea ice thickness (Zhang and Rothrock, 2003).

Different from Y20, in this study, we change the localization radius from 2 to 6 grids during the assimilation procedures to reduce some instability during initial Arctic sea ice simulations associated with 2 localization radii. As shown in Supplementary Figure S1, the ice thickness with 2 localization radii and 1.5 m uncertainty (used in Y20) shows some discontinuous features (Fig. S1a), which tend to result in numerical instability during the initial

integration. Such discontinuous features are obviously corrected with 6 localization radii and 0.75 m uncertainty (Fig. S1b). Following Y20, here we test the 2018 prediction experiment with 6 localization radii for the data assimilation, which shows very similar temporal evolution of the total Arctic sea ice extent for the July experiment relative to that of Y20, although it (red solid line) predicts slightly less ice extent than that of Y20 (blue line) (Supplementary Figure S2). In this study, this configuration is designated as the reference for the following assessment of the updated CAPS (hereafter Y20_MOD).

For the evaluation of Arctic sea ice prediction, Sea Ice Index (Fetterer et al., 2017; obtained from https://nsidc.org/data/G02135) is used as the observed total sea ice extent, and the NSIDC sea ice concentrations (SIC) derived from Special Sensor Microwave Imager/Sounder (SSMIS) with the NASA Team algorithm (Cavalieri et al., 1996; obtained from https://nsidc.org/data/nsidc-0051) is also used. For the assessment of the simulated atmospheric and oceanic variables, the European Centre for Medium-Range Weather Forecasts (ECMWF) reanalysis version 5 (ERA5; Hersbach et al., 2020; obtained from https://cds.climate.copernicus.eu) and National Oceanic and Atmospheric Administration (NOAA) Optimum Interpolation (OI) Sea Surface Temperature (SST) (Reynolds et al., 2007; obtained from https://psl.noaa.gov/data/gridded/data.noaa.oisst.v2.highres.html) are utilized. For the comparison of spatial distribution, SIC, ERA5, and OISST are interpolated to the model grid.

3. Evaluation of updated CAPS

3.1. Experiment designs and methodology

The model domain includes 319 (449) x- (y-) grid points with a ~24 km grid spacing for all model components (see Figure 2 in Y20). The WRF model uses 50 vertical levels, the ROMS model uses 40 vertical levels, and the CICE model uses 7 ice layers, 1 snow layer, and 5 categories of sea ice thickness. The coupling frequency across all model components is 30 minutes. Initial and boundary conditions for the WRF and ROMS models are generated from the Climate Forecast System version 2 (CFSv2, Saha et al., 2014) operational forecast archived at NCEP (http://nomads.ncep.noaa.gov/pub/data/nccf/com/cfs/prod/). Sea ice initial conditions are generated from the data assimilation described in section 2. Ensemble predictions with 8 members are conducted. A set of numerical experiments for the Pan-Arctic seasonal sea ice prediction with different physics, starting from July 1st to October 1st for the year of 2018, has been conducted. Table 2 provides the details of these experiments that allow us to examine physical processes linking improved/changed physical parameterizations in the updated CAPS to Arctic sea ice simulation and prediction.

In this study, sea ice extent is calculated as the sum of area of all grid cells with ice concentration greater than 15%. Besides the total Arctic sea ice extent, we also calculate the ice extent for the following subregions: 1) Beaufort and Chukchi Seas (120°W-180, 60°N-80°N), 2) East Siberian and Laptev Seas (90°E-180, 60°N-80°N), and 3) Barents, Kara, and Greenland Seas (30°W-90°E, 60°N-80°N). To further assess the predictive skill of Arctic sea ice predictions, we show the climatology prediction (CLIM, the period of 1998-2017) and the damped anomaly persistence prediction (DAMP). Following Van den Dool (2006), the DAMP prediction is generated from the initial sea ice extent anomaly (relative to the 1998-2017

climatology) scaled by the autocorrelation and the ratio of standard deviation between different lead times and initial times (see the DAMP equation in Y20).

In order to understand physical contributors that drive the evolution of Arctic sea ice state (the standard variables of the ice concentration and thickness), the mass budget of Arctic sea ice for all experiments is analyzed in this study as defined in Notz et al. (2016, Append. E), including:

- sea ice growth in supercooled open water (frazil)
- sea ice growth at the bottom of the ice (basal growth)
- sea ice growth due to transformation of snow to sea ice (snowice)
- sea ice melt at the air-ice interface (top melt)
- sea ice melt at the bottom of the ice (basal melt)
- sea ice melt at the sides of the ice (lateral melt)
- sea ice mass change due to dynamics-related processes (e.g. advection) (dynamics)

These diagnostic variables are determined by saving the ice mass tendency of above processes separately every time step and integrated to output the daily-mean value.

3.2. Impacts of the RAP physics in the WRF model

To examine the performance of the upgrades of physical parameterization in component models in CAPS one step at a time compared to its predecessor in Y20, we define the Y21_CTRL experiment that uses the RAP physics in the WRF model (see Table 2 for differences between Y21_CTRL and Y20_MOD). Recently, the Rapid Refresh (RAP) model, a high-frequency weather prediction/assimilation modeling system operational at the National

Centers for Environmental Prediction (NCEP), has made some improvements in the WRF model physics (Benjamin et al., 2016), including improved Grell-Freitas convection scheme (GF) and Mellor-Yamada-Nakanishi-Niino planetary boundary layer scheme (MYNN). For the GF scheme, the major improvements relative to the original scheme (Grell and Freitas, 2014) include: 1) a beta probability density function used as the normalized mass flux profile for representing height-dependent entrainment/detrainment rates within statistical-averaged deep convective plumes, which is given as:

$$Z_{u,d}(r_k) = c r_k^{\alpha} - (1 - r_k)^{\beta} - 1$$

where $Z_{u,d}$ is the mass flux profiles for updrafts and downdrafts, c is a normalization constant, r_k is the location of the mass flux maximum, α and β determine the skewness of the beta probability density function, and 2) the ECMWF approach used for momentum transport due to convection (Biswas et al. 2020; Freitas et al. 2018; 2021). For the MYNN scheme, the RAP model improves the mixing-length formulation, which is designed as:

$$\frac{1}{l_m} = \frac{1}{l_s} + \frac{1}{l_t} + \frac{1}{l_b}$$

where l_m is the mixing length, l_s is the surface length, l_t is the turbulent length, and l_b is the buoyancy length. Compared to the original scheme, the RAP model changed coefficients in the formulation of l_s, l_t, and l_b for reducing the near-surface turbulent mixing, and the diffusivity of the scheme. The RAP model also removes numerical deficiencies to better represent subgrid-scale cloudiness (Benjamin et al. 2016, see Append. B) compared to the original scheme (Nakanishi and Nino, 2009). In addition, some minor issues in the Noah land surface model (Chen and Dudhia, 2001) have been fixed, including discontinuous behavior for

246 soil ice melting, negative moisture fluxes over glacial, and associated with snow melting.

247 Apparently, the above RAP physics can have influence on the behavior of simulated
248 atmospheric thermodynamics (i.e., radiation, temperature). Figure 1 and 2 show the spatial
249 distribution of the ERA5 surface downward solar and thermal radiation (SWDN and LWDN),
250 the prediction errors (ensemble mean minuses ERA5) of Y20_MOD, and the difference
251 between Y21_CTRL and Y20_MOD. For July, Y20_MOD (Fig. 1d) results in less SWDN over
252 most of ocean basins as well as Alaska and northeast US, western Siberia, and eastern Europe,
253 but more SWDN over southern and eastern Siberia compared with ERA5. For August and
254 September (Fig. 1e-f), the spatial distribution is generally similar to that of July, except that
255 eastern Siberia (less SWDN) and northern Canada (more SWDN) in August. It appears that the
256 magnitude of the prediction errors tends to decrease over the areas with large prediction errors
257 as the prediction time increases (i.e., July vs. September). Compared with Y20_MOD, the RAP
258 physics in Y21_CTRL results in large areas with smaller prediction errors in July (e.g., the
259 positive difference between Y21_CTRL and Y20_MOD reduces the negative prediction errors
260 in Y20_MOD), except the north Pacific (especially the Sea of Okhotsk) and north Canada (Fig.
261 1g). For August and September (Fig. 1h, i), encouragingly, there are more areas with smaller
262 prediction errors.

263 In contrast to SWDN, the prediction errors of LWDN in Y20_MOD have much smaller
264 magnitude (up to 100 W/m^2 in SWDN vs. 50 W/m^2 in LWDN) for the entire prediction period
265 (Fig. 2d-f). For July, Y20_MOD (Fig. 2d) simulates less LDWN over most of the model domain
266 compared with ERA5, except the Atlantic sector and north Greenland. For August, the areas

with negative prediction errors expand and the magnitude of prediction errors increases (particularly in southeastern Siberia and northeast US) compared to that of July (Fig. 2e). For September (Fig. 2f), the spatial distribution of LWDN is mostly similar to that of July, except that north Canada and Canadian Archipelago show positive prediction errors. The Y21_CTRL experiment with the RAP physics tends to reduce the prediction errors in Y20_MOD, especially over eastern Siberia and the Atlantic sector in July to September (Fig. 2g-i). However, Y21_CTRL results in larger bias in the central Northern Atlantic in August than that of Y20_MOD (Fig. 2h).

Figure 3 shows the spatial distribution of the ERA5 2m air temperature, the prediction errors of Y20_MOD, and the difference between Y21_CTRL and Y20_MOD. For Y20_MOD, the predicted air temperature in July has small cold prediction errors over all ocean basins, small-to-moderate cold prediction errors (~3-5 degrees) over Canada and Siberia, and moderate-to-large cold prediction errors (~6-9 degrees) over eastern Europe (Fig. 3d). In August (Fig. 3e), the cold prediction errors over most of the model domain are increased, in particular, very large cold prediction error (over 10 degrees) is located over east Siberia. In September, these cold prediction errors are decreased relatively, and some warm prediction errors are found in north of Greenland (Fig. 3f). With the adaptation of the RAP physics in the WRF model, Y21_CTRL, in general, produces a warmer state in most of the model domain compared to that of Y20_MOD during the entire prediction period. For July (Fig. 3g), the predicted air temperature is slightly warmer over the Arctic Ocean, the Pacific, and Atlantic sectors, moderately warmer (~1-2 degrees) over central and eastern Siberia and Canadian

Archipelago, but the slightly colder over northern Canada than that of Y20_MOD. For August and September (Fig. 3h), most of the model domain is warmer in Y21_CTRL than that of Y20_MOD, in particular excessive cold prediction errors shown in Y20_MOD over Siberia are reduced notably (~2.5-4 degrees). We notice that the RAP physics does not have significant impacts on atmospheric circulations, given that Y21_CTRL and Y20_MOD have very similar wind patterns (not shown).

Figure 4 shows the temporal evolution of the ensemble mean of the predicted Arctic sea ice extent along with the NSIDC observations. In terms of total ice extent, compared to the Y20_MOD experiment (blue line), the Y21_CTRL experiment (yellow line) produces ~0.5 million km^2 more ice extent at the initial. Note that the difference in the initial ice extent is related to that sea ice fields in Y20_MOD and Y21_CTRL (as well as other experiments listed in Table 2) are initialized based on one-month free runs (section 2), which use different physical configurations listed in Table 2. These one-month free runs do not have the same evolution in sea ice fields and result in different initial ice fields after data assimilation. The ice extent in Y21_CTRL decreases faster than Y20_MOD during the first 2-week integration. After that, they track each other closely, and predict nearly the same minimum ice extent (~4.3 million km^2). Like Y20_MOD, Y21_CTRL still has a delayed ice recovery in late September compared to the observations. Compared with the CLIM/DAMP predictions (black dashed and dotted lines), both Y20_MOD and Y21_CTRL have smaller prediction errors in August, but comparable prediction errors after early September.

The difference in sea ice extent becomes larger at regional scales, in the East Siberian-

Laptev Seas, Y21_CTRL shows faster ice decline after mid-July than that of Y20_MOD, whereas in the Beaufort-Chukchi Seas, Y21_CTRL predicts slower ice retreat after late July than that of Y20_MOD (Fig. 4a, 4b). They are consistent with that Y21_CTRL predicts warmer (relatively colder) temperature than that of Y20_MOD in the East Siberian-Laptev (Beaufort-Chukchi) Seas. Both Y20_MOD and Y21_CTRL agree well with the observations in the Barents-Kara-Greenland Seas (Fig. 4c). Compared with the observations, Y20_MOD performs relatively better in regional ice extents than that of Y21_CTRL. Figure 5 shows the spatial distribution of the NSIDC sea ice concentration and the difference between the predicted ice concentration and the observations for all grid cells that the predictions and the observations both have at least 15% ice concentration. The vertical and horizontal lining areas represent difference of the ice edge location. Like regional ice extent shown in Figure 4, Y21_CTRL predicts lower (higher) ice concentration along the East Siberian-Laptev (Beaufort-Chukchi) Seas (Fig. 5e_1-e_3). Y21_CTRL also predicts less ice in the central Arctic Ocean in August and September, which is consistent with warmer temperature in Y21_CTRL relative to Y20_MOD.

Figure 6 shows the evolution of sea ice mass budget terms of Y20_MOD and Y21_CTRL, averaged with cell-area weighting over the entire model domain. During the entire prediction period, most of the ice loss in Y20_MOD and Y21_CTRL are caused by basal melting. The surface melting has relatively small contribution in the total ice loss and mainly occurs in July. However, compared with Y20_MOD (Fig. 6a), Y21_CTRL (Fig. 6b) shows much larger magnitude for basal and surface melt. In a fully coupled predictive model, the changes of sea ice are determined by the fluxes from the atmosphere above and the ocean below. Associated

with the increased downward radiation of the above RAP physics, Y21_CTRL absorbs more shortwave radiation (SWABS, Fig. 7a) and allows more penetrating solar radiation into the upper ocean below sea ice (SWTHRU, Fig. 7b) than that of Y20_MOD, especially in July. This explains why Y21_CTRL has larger magnitude of surface and basal melting terms. Although Y21_CTRL show larger magnitude in surface and basal melting than that of Y20_MOD, the ice extent in Y21_CTRL and Y20_MOD shown in Figure 4 show similar evolution. The effect of larger surface and basal melting in Y21_CTRL is largely reflected in the ice thickness change. As shown in Figure S3, Y21_CTRL has thinner ice thickness than that of Y20_MOD, in the East Siberian-Laptev Seas in July and in the much of central Arctic Ocean in August and September.

3.3. Impacts of the tracer advection in ROMS model

Currently, the ROMS model that uses a generalized topography-following coordinate has two vertical coordinate transformation options:

$$z(x,y,\sigma,t) = S(x,y,\sigma) + \zeta(x,y,t)\left[1 + \frac{S(x,y,\sigma)}{h(x,y)}\right] \quad (1)$$
$$S(x,y,\sigma) = h_c\sigma + [h(x,y) - h_c]C(\sigma)$$

or

$$z(x,y,\sigma,t) = \zeta(x,y,t) + [\zeta(x,y,t) + h(x,y)]S(x,y,\sigma)$$
$$S(x,y,\sigma) = \frac{h_c\sigma + h(x,y)C(\sigma)}{h_c + h(x,y)} \quad (2)$$

where $S(x,y,\sigma)$ is a nonlinear vertical transformation function, $\zeta(x,y,t)$ is the free-surface, $h(x,y)$ is the unperturbed water column thickness, $C(\sigma)$ is the non-dimensional, monotonic, vertical stretching function, and h_c controls the behavior of the vertical stretching. In Y20, we

used the transformation 1 and the vertical stretching function introduced by Song and Haidvogel (1994). However, the vertical transformation 1 has an inherent limitation for the value of h_c (expected to be the thermocline depth), which must be less than or equal to the minimum value in $h(x,y)$. As a result, h_c was chosen as 10 meters due to the limitation of the minimum value in $h(x,y)$ in Y20. This limitation is removed with the vertical transformation 2 and h_c can be any positive value. Here the Y21_VT experiment is conducted to examine the impact of the vertical transformation in the ROMS model on seasonal Arctic sea ice simulation and prediction, which uses the vertical transformation 2, the Shchepetkin vertical stretching function (a function introduced in a research version of ROMS at University of California, Los Angeles), and 300 meters for h_c. As shown in Supplementary Figure S4-S5, compared to Y21_CTRL, Y21_VT is less sensitive to the bathymetry and its layers are more evenly-distributed in the upper 300 meters. With the changes of vertical layers of the upper ocean, the Y21_VT experiment has minor SST changes relative to Y21_CTRL. The simulated temporal evolution of total ice extent of Y21_VT (Fig. 4, red line) resembles to that of Y21_CTRL (Fig. 4, yellow line), although some differences are seen at the regional scale in the areas with shallow water (e.g., East Siberian, Laptev, Barents, and Kara Seas). The configuration of Y21_VT is used in the following experiments.

It has been recognized that the tracer advection and the vertical mixing schemes have important effects on ocean and sea ice simulation (e.g., Liang and Losch, 2018; Naughten et al., 2017). Here the Y21_RP experiment is designated to explore the influence of different advection schemes in the ROMS model. Specifically, the tracer advection scheme is changed

371 from the Multidimensional positive definite advection transport algorithm (MPDATA;
372 Smolarkiewicz, 2006) to the third-order upwind horizontal advection (U3H; Rasch, 1994;
373 Shchepetkin, and McWilliams, 2005) and the fourth-order centered vertical advection schemes
374 (C4V; Shchepetkin, and McWilliams, 1998; 2005). The MPDATA scheme applied in
375 Y20_MOD, Y21_CTRL, and Y21_VT is a non-oscillatory scheme but a sign preserving
376 scheme (Smolarkiewicz, 2006). This means MPDATA is not suitable for tracer fields having
377 both positive and negative values (i.e., temperature with degree Celsius in the ROMS model).
378 The upwind third-order (U3H) scheme used in Y21_RP is an oscillatory scheme but it
379 significantly reduces oscillations compared to other centered schemes (e.g., Hecht et al., 2000;
380 Naughten et al., 2017) available in the ROMS model.

381 Figure 8 shows the spatial distribution of the SST changes of Y21_VT and Y21_RP
382 relative to Y21_CTRL (as well as the OISST and the difference between Y21_CTRL and
383 OISST). In general, Y21_CTRL shows cold prediction errors in the North Pacific (~2 degrees)
384 and the Atlantic (~3 degrees) compared to that of OISST in July, and these cold prediction
385 errors are enhanced as the prediction time increases (to 3-5 degrees, Fig. 8d-f). With the
386 U3H/C4V tracer advection scheme in Y21_RP, cold prediction errors shown in Y21_CTRL are
387 reduced significantly in the north Pacific and Atlantic, but SST under sea ice in much of the
388 Arctic Ocean is slightly colder than that of Y21_CTRL (Fig. 8j-l).

389 Y21_RP (Fig. 4, green line) shows comparable temporal evolution of the ice extent as
390 Y21_CTRL (as well as Y21_VT) until near the end of July. After that, the ice melting slows
391 down (closer to the observations) and the ice extent begins to recover earlier (after the first

week of September) in Y21_RP compared to that of Y21_CRTL. This leads to much smaller prediction error in seasonal minimum ice extent relative to the observation. Y21_RP also shows better predictive skill after late August compared with the CLIM/DAMP predictions (black dashed and dotted lines). This suggests the delayed ice recovery in late September shown in Y20_MOD, Y21_CTRL and Y21_VT is in part due to the choice of ocean advection and vertical mixing schemes, which change the behavior of ocean state. At the regional scale, the slower ice decline after July and earlier recovery of the ice extent in September mainly occur in the Beaufort-Chukchi and Barents-Kara-Greenland Seas compared to that of Y21_CTRL (Fig. 4a, c). With U3H/C4V scheme, the Y21_RP experiment simulates higher sea ice concentration than that of Y21_VT (Fig. 5f_1-f_3). For September, the Y21_RP experiment better predicts the ice edge location in the Atlantic sector of the Arctic (i.e., smaller areas with horizontal/vertical lining) compared to the experiments described above (not shown).

Figure 9 shows the evolution of sea ice mass budget terms of Y21_VT and Y21_RP. Relative to Y21_VT, Y21_RP (with U3H/C4V scheme) results in increased frazil ice formation in July, which is partly compensated by increased surface melting. Y21_RP also leads to increased basal growth in mid- and late September (Fig. 9a, b).

Figure 10 shows the difference in the vertical profile of ocean temperature and salinity in the upper 150 m averaged for the central Arctic Ocean between Y21_RP and Y21_VT. The ocean temperature in the surface layer of Y21_RP is slightly colder during the prediction period compared to that of Y21_VT (Fig. 10a), especially in August and September. Moreover, the water in the surface layer (0-20 m) of Y21_RP is fresher than that of Y21_VT (Fig. 10b). It

reduces the freezing temperature and favors frazil ice formation. In CAPS, frazil ice formation is determined by the freezing potential, which is the vertical integral of the difference between temperature in upper ocean layer and the freezing temperature in the upper 5 m-layer. The temperature of supercooled water is adjusted based on the freezing potential to form new ice and rejects brine into the ocean that leads to saltier water between 20-50 m in Figure 10. It should be noted that the increased frazil ice formation in July in Y21_RP might be also the results of model adjustment and/or numerical error. The oscillatory behavior of U3H scheme can make the temperature fall below the freezing point and then instantaneously forms new ice (as well as temperature/salinity adjustments).

3.4. Impacts of sea ice thermodynamics in the CICE model

In Y20, we used sea ice thermodynamics introduced by Bitz and Lipscomb (1999; hereafter BL99) as the setup of CAPS, which assumes a fixed vertical salinity profile based on observations. The new CICE model includes a MUSHY-layer ice thermodynamics introduced by Turner et al. (2013), which simulates vertically and time-varying prognostic salinity and associated effects on thermodynamic properties of sea ice. In the Y21_MUSHY experiment, we change the ice thermodynamics from BL99 to MUSHY (Table 2) to examine whether improved ice thermodynamics has noticeable influence on Arctic sea ice simulation and prediction at seasonal timescale. Compared to Y21_RP, Y21_MUSHY (Fig. 4, pink line) produces very similar evolution of total ice extent. However, it simulates relatively larger ice extent near the end of September, which is also reflected by the basin-wide increased ice cover shown in Figure 5h$_3$. At the regional scale, compared to Y21_RP, Y21_MUSHY predicts less

ice in August in the Beaufort-Chukchi. The opposite is the case for the East Siberian-Laptev Seas (Fig. 4a, b).

Figure 11 shows the difference of the ensemble mean of the predicted ice thickness between Y21_MUSHY and Y21_RP. Compared with Y21_RP, Y21_MUSHY simulates thicker ice (from ~0.2m in July to over 0.4m in September) extending from the Canadian Arctic, through the central Arctic Ocean, to the Laptev Sea (Fig. 11a-c). This seems to be consistent with previous studies, which show that the Mushy-layer thermodynamics simulates thicker ice than BL99 thermodynamics in both standalone CICE (Turner and Hunke, 2015) and the fully-coupled (Bailey et al., 2020), but Y21_MUSHY shows thinner ice (~0.2m) in an arc extending from north of Alaska to north of eastern Siberia compared to Bailey et al. (2020). Note that Y21_MUSHY focuses the effects of Mushy-thermodynamics on seasonal timescale while the results in Bailey et al. (2020) are based on 50-year simulations.

Compared to Y21_RP, the mass budget of Y21_MUSHY (Fig. S6) shows that both surface melting and frazil ice formation terms are increased. This compensation between surface melting and frazil ice formation from the Mushy-layer thermodynamics in CAPS leads to relatively unchanged total ice extent between Y21_MUSHY and Y21_RP (Fig. 4 green and pink lines).

4. Prediction skill of CAPS at longer timescale

The design of Arctic sea ice prediction experiments described above follow the protocol of the Sea Ice Prediction Network (SIPN), in which the outlook start from June 1st, July 1st, and

August 1st to predict seasonal minimum of the ice extent in September. It is not clear that how predictive skills of dynamical models participating in SIPN may change for longer period. Here we conduct two more experiments to investigate the predictive capability of CAPS beyond the SIPN prediction period. For the prediction experiments discussed above, we use a simple approach to merge CryoSat-2 and SMOS ice thickness by replacing ice thickness less than 1m in CryoSat-2 data with SMOS data for ice thickness assimilation. Ricker et al. (2017) presented a new ice thickness product (CS2SMOS) based on the optimal interpolation to statistically merge CrySat-2 and SMOS data. Here we utilize the configuration of Y21_RP but use CS2SMOS SIT for the assimilation (Y21_SIT; Table 2). The predicted total ice extent is almost identical to Y21_RP in July but slightly larger total extent after July than that of Y21_RP (not shown). The configuration of Y21_SIT is used in the following experiments. Taking advantage of the entire prediction period provided by CFS forecasts (7 months), the Y21_EXT-7 experiment is designed to extend the prediction period to the end of January next year (Table 2). Figure 12 shows the temporal evolution of the ensemble mean of the predicted total Arctic sea ice extent (as well as regional ice extent) for Y21_EXT-7. Total ice extent of Y21_EXT-7 exhibits reasonable evolution in terms of seasonal minimum and timing of recovery compared with the observations until late November. Y21_EXT-7 also performs better than that of the CLIM/DAMP predictions (black dashed and dotted lines) until mid-to-late November. After that, Y21_EXT-7 overestimates total ice extent relative to the observations, and such overestimation is largely contributed by more extensive sea ice in the Barents-Kara-Greenland Seas (Fig. 12c), which is a result of a sharp increase in the basal growth term after mid-to-late

November (not shown).

5. Conclusions and Discussions

This paper presents and evaluates the updated Coupled Arctic Prediction System (CAPS) designated for Arctic sea ice prediction through a case study for the year of 2018. A set of Pan-Arctic prediction experiments with improved/changed physical parameterizations as well as different configurations starting from July 1st to the end of September are performed for 2018 to assess their impacts of the updated CAPS on the predictive skill of Arctic sea ice at seasonal timescale. Specifically, we focus on the Rapid Refresh (RAP) physics in the WRF model, the oceanic tracer advection scheme in the ROMS model, sea ice thermodynamics in the CICE model, and investigate physical processes linking them to Arctic sea ice simulation and prediction.

The results show that the updated CAPS with improved physical parameterizations can better predict the evolution of total ice extent compared with its predecessor described in Yang et al. (2020), though the predictions exhibit some prediction errors in regional ice extent. The key improvements of WRF, including cumulus, boundary layer, and land surface schemes, result in improved simulations in downward radiative fluxes and near surface air temperature. These improvements mainly influence the predicted ice thickness instead of total ice extent. The difference in the predicted ice thickness can have potential impacts on the icebreakers planning their routes across the ice-covered regions. The major changes of ROMS, including tracer advection and vertical mixing schemes, reduces the prediction errors in sea surface temperature and changes ocean temperature and salinity structure in the surface layer, leading

to improved evolution of the predicted total ice extent (particularly correcting the late ice recovery issue in the previous CAPS). The changes of CICE, including improved ice thermodynamics, have noticeable influences on the predicted ice thickness.

We demonstrate that CAPS can remain skillful beyond the designated period of Sea Ice Prediction Network (SIPN), which has potential values for stakeholders to make decisions regarding the socioeconomical activities in the Arctic. Although CAPS shows extended predictive skill to the freeze-up period, the prediction produces extensive ice through the basal growth near the end of prediction. The excessive basal growth may be partly due to that the bias of the CFS data propagates into the model domain through lateral boundary conditions and its accumulated effect influences Arctic sea ice simulation during the freeze-up period.

Keen et al. (2021) analyzed the Arctic mass budget of 15 models participated in the Coupled Model Intercomparison Project Phase 6 (CMIP6). We notice that, first, the top melting and the basal melting terms in CMIP6 models have comparable contributions in July while the top melting term only has ~50% contribution relative to the basal melting term in CAPS. The updated CAPS with the RAP physics improves the performance of shortwave/longwave radiation at the surface (Fig. 1 and Fig. 2). The net flux at the ice surface, however, may still be underestimated in the updated CAPS. Besides, the surface property of sea ice (i.e., the amount of melt ponds, bare ice, and snow) is a factor that influences surface albedo and thus the absorbed shortwave radiation (e.g., Nicolaus et al., 2012; Nicolaus and Katlein, 2013). The prediction experiments starting at July 1st in this study do not consider the initialization of melt ponds (i.e., zero melt pond coverage at the initial). However, melt ponds start to develop in

early May based on the satellite observations (e.g., Liu et al., 2015, Fig. 1). The initialization of melt pond based on the observations (e.g., Ding et al., 2020) in CAPS is a direction to improve the representation of the ice surface properties. Second, the mass budget analysis by both Keen et al. (2021) and this study show that the contribution of lateral melting term is relatively small, which might be due to that CMIP6 models and CAPS assume constant floe-size (i.e., 300 meters in CICE), which is a critical value to determine the strength of lateral melting (e.g., Horvat et al., 2016; Steele, 1992). Recently, several studies have proposed floe size distribution models (e.g., Bateson et al., 2020; Bennetts et al., 2017; Boutin et al., 2020; Horvat and Tziperman, 2015; Roach et al., 2018, 2019; Zhang et al., 2015, 2016). Incorporating floe size distribution model in CAPS and understanding its impacts on seasonal Arctic sea ice prediction will be a future direction of developing CAPS. Lastly, the prediction experiments with the upwind advection scheme (i.e., Y21_RP, Y21_EXT-7) shows spurious large frazil ice formation, particularity in July, which is different from the analysis shown in Keen et al. (2021). An approach for reducing spurious frazil ice formation is proposed by Naughten et al. (2017) that they implemented upwind flux limiter (Leonard and Mokhtari, 1990) to the U3H scheme to further reduce the oscillations. Naughten et al. (2018) also suggested that the oscillatory behaviors can be smoothed out by applying the Akima fourth-order tracer advection scheme combined with Laplacian horizontal diffusion at a level strong enough. Beside of the oscillatory behaviors of advection scheme, the ice-ocean heat flux may also play a role in the spurious frazil ice formation. As discussed in section 3.3, the freezing/melting potential not only determines the amount of newly-formed ice, but also limits the amount of energy that can be

539 extracted from the ocean surface layer to melt sea ice. This implies that the ocean surface layer
540 will be close to the freezing temperature if the ice-ocean heat fluxes reach the limit imposed by
541 the melting potential. Shi et al. (2021) discussed the impacts of different ice-ocean heat flux
542 parametrizations on sea ice simulations. Their results suggest that Arctic sea ice will be thicker
543 and ocean temperature will warmer beneath high-concentration ice with a complex approach
544 proposed by Schmidt et al. (2004) that limits melt rates (heat fluxes) of sea ice through
545 considering a fresh water layer underlying sea ice. The warmer ocean temperature under sea
546 ice with a more complex approach in parameterizing ice-ocean heat flux may be the solution
547 to reduce the occurrence of local temperature falling below freezing temperature with
548 oscillatory advection schemes.

549 Based on the prediction experiments discussed in this paper, the configuration with the
550 RAP physics, the U3H/C4V ocean advection, BL99 ice thermodynamics, and CS2SMOS ice
551 thickness assimilation (Table 2, Y21_SIT) is assigned as the finalized CAPS version 1.0.
552 Improving the representation of physical processes in CAPS version 1.0 for further reducing
553 the model bias will remain the main focus for the development of CAPS. Since CAPS is a
554 regional modeling system, it relies on the forecasts form global climate models as initial and
555 lateral boundary conditions. That is, biases existed in GCM simulations (here the CFS forecast)
556 can be propagated into and affect the entire area-limited domain (e.g., Bruyère et al., 2014;
557 Rocheta et al., 2020; Wu et al., 2005). This issue can be a potential source that influences the
558 predictive capability of CAPS for longer timescales. Studies have applied bias correction
559 techniques with different complexities for improving the performance of regional modeling

560 system (e.g., Bruyère et al., 2014; Colette et al., 2012; Rocheta et al., 2017, 2020). Further
561 investigation is needed to address biases inherited from GCM predictions through lateral
562 boundaries for improving the predictive capability of CAPS.
563

Code and data availability: The COAWST and CICE models are open source and can be downloaded from their developers at https://github.com/jcwarner-usgs/COAWST and https://github.com/CICE-Consortium/CICE, respectively. PDAF can be obtained from https://pdaf.awi.de/trac/wiki. CAPS v1.0 described in this paper is permanently archived at https://doi.org/10.5281/zenodo.5034971. The prediction data analyzed in this paper can be accessed from https://doi.org/10.5281/zenodo.4911415.

Author contributions: CYY and JL designed the model experiments, developed the updated CAPS model, and wrote the manuscript, CYY conducted the prediction experiments and analyzed the results. DC provided constructive feedback on the manuscript.

Competing interests: The authors declare that they have no conflict of interest.

Acknowledgements: This research is supported by the National Key R&D Program of China (2018YFA0605901), the National Natural Science Foundation of China (42006188 and 41922044), and the Innovation Group Project of Southern Marine Science and Engineering Guangdong Laboratory (Zhuhai) (311021008). The authors also acknowledge the National Centers for Environmental Prediction for providing CFS seasonal forecasts, the University of Hamburg for distributing the SMOS sea ice thickness data, the Alfred-Wegener-Institut, Helmholtz Zentrum für Polar- und Meeresforschung for providing the CryoSat-2 sea ice thickness data and CS2SMOS data, the Polar Science Center for distributing the PIOMAS ice thickness data, the National Snow and Ice Data Center for providing the SSMIS sea ice concentration data, the European Centre for Medium-Range Weather Forecasts for distributing the ERA5 reanalysis, and the National Oceanic and Atmospheric Administration for providing the OI sea surface temperature.

6. References

Aagaard, K.: A synthesis of the Arctic Ocean circulation. Rapp. P.-V. Reun.- Cons. Int. Explor. Mer, 188, 11–22, 1989.

Bailey, D. A., Holland, M. M., DuVivier, A. K., Hunke, E. C., and Turner, A. K.: Impact of a new sea ice thermodynamic formulation in the CESM2 sea ice component. Journal of Advances in Modeling Earth Systems, 12, e2020MS002154. https://doi.org/10.1029/2020MS002154, 2020.

Bateson, A. W., Feltham, D. L., Schröder, D., Hosekova, L., Ridley, J. K., and Aksenov, Y.: Impact of sea ice floe size distribution on seasonal fragmentation and melt of Arctic sea ice, The Cryosphere, 14, 403–428, https://doi.org/10.5194/tc-14-403-2020, 2020.

Bitz, C. M. and Lipscomb, W. H.: An energy-conserving thermodynamic sea ice model for climate study. J. Geophys. Res.-Oceans, 104, 15669–15677, 1999.

Benjamin, S. G., Weygandt, S. S., Brown, J. M., Hu, M., Alexander, C. R., Smirnova, T. G. and Manikin, G. S.: A North American hourly assimilation and model forecast cycle: the Rapid Refresh. Monthly Weather Review, 144,1669–1694. https://doi.org/10.1175/MWR-D-15-0242.1, 2016.

Bennetts, L. G., O'Farrell, S., and Uotila, P.: Brief communication: Impacts of ocean-wave-induced breakup of Antarctic sea ice via thermodynamics in a stand-alone version of the CICE sea-ice model, The Cryosphere, 11, 1035–1040, https://doi.org/10.5194/tc-11-1035-2017, 2017.

Biswas, M. K., Zhang, J. A., Grell, E., Kalina, E., Newman, K., Bernardet, L., Carson, L., Frimel, J., and Grell, G.: Evaluation of the Grell–Freitas Convective Scheme in the Hurricane Weather Research and Forecasting (HWRF) Model, Weather and Forecasting, 35(3), 1017-1033, 2020.

Blanchard-Wrigglesworth, E., Bitz, C., and Holland, M.: Influence of initial conditions and climate forcing on predicting Arctic sea ice. Geophysical Research Letters, 38, L18503. https://doi.org/10.1029/2011GL048807, 2011.

Blanchard-Wrigglesworth, E., and Bushuk, M.: Robustness of Arctic sea-ice predictability in GCMs. Climate Dynamics, 52, 5555–5566, 2018.

Blanchard-Wrigglesworth, E., Cullather, R., Wang, W., Zhang, J., and Bitz, C. M.: Model forecast skill and sensitivity to initial conditions in the seasonal sea ice outlook. Geophysical Research Letters, 42, 8042–8048. https://doi.org/10.1002/2015GL065860, 2015.

Boutin, G., Lique, C., Ardhuin, F., Rousset, C., Talandier, C., Accensi, M., and Girard-Ardhuin, F.: Towards a coupled model to investigate wave–sea ice interactions in the Arctic marginal ice zone, The Cryosphere, 14, 709–735, https://doi.org/10.5194/tc-14-709-2020, 2020.

Briegleb, B. P. and Light, B.: A Delta-Eddington multiple scattering parameterization for solar radiation in the sea ice component of the Community Climate System Model. NCAR Tech. Note NCAR/TN-472+STR, National Center for Atmospheric Research, 2007.

Bruyère, C. L., Done, J. M., Holland, G. J., and Fredrick, S.: Bias corrections of global models for regional climate simulations of high-impact weather. Clim Dyn 43, 1847–1856 (2014). https://doi.org/10.1007/s00382-013-2011-6, 2014.

Carmack, E., Polyakov, I., Padman, L., Fer, I., Hunke, E., Hutchings, J., Jackson, J., Kelley, D., Kwok, R., Layton, C., Melling, H., Perovich, D., Persson, O., Ruddick, B., Timmermans, M.-L., Toole, J., Ross, T., Vavrus, S., and Winsor, P.: Toward Quantifying the Increasing Role of Oceanic Heat in Sea Ice Loss in the New Arctic. Bulletin of the American Meteorological Society 96, 12, 2079-2105, https://doi.org/10.1175/BAMS-D-13-00177.1, 2015.

Cavalieri, D. J., Parkinson, C. L., Gloersen, P., and Zwally, H. J.: updated yearly. Sea Ice Concentrations from Nimbus-7 SMMR and DMSP SSM/I-SSMIS Passive Microwave Data, Version 1. Boulder, Colorado USA. NASA National Snow and Ice Data Center Distributed Active Archive Center. https://doi.org/10.5067/8GQ8LZQVL0VL, 1996.

642 Chen, F. and Dudhia, J.: Coupling an advanced land surface–hydrology model with the Penn
643 State–NCAR MM5 modeling system. Part I: Model implementation and sensitivity. Mon.
644 Wea. Rev., 129, 569–585, 2001.
645 Chevallier, M., Salas y Mélia, D., Voldoire, A., Déqué, M., and Garric, G.: Seasonal forecasts
646 of the pan-Arctic sea ice extent using a GCM-based seasonal prediction system. Journal
647 of Climate, 26(16), 6092–6104, 2013.
648 Colette, A., Vautard, R., and Vrac, M.: Regional climate downscaling with prior statistical
649 correction of the global climate forcing, Geophys. Res. Lett., 39, L13707,
650 https://doi.org/10.1029/2012GL052258, 2012.
651 Day, J. J., Tietsche, S., Collins, M., Goessling, H. F., Guemas, V., Guillory, A., et al.: The
652 Arctic predictability and prediction on seasonal-to-interannual timescales (apposite) data
653 set version 1. Geoscientific Model Development, 9, 2255–2270, 2016.
654 Ding, Y., Cheng, X., Liu, J., Hui, F., Wang, Z., and Chen, S.: Retrieval of Melt Pond Fraction
655 over Arctic Sea Ice during 2000–2019 Using an Ensemble-Based Deep Neural Network.
656 Remote Sensing. 12(17):2746. https://doi.org/10.3390/rs12172746, 2020
657 DuVivier, A. K., Holland, M. M., Landrum, L., Singh, H. A., Bailey, D. A., and Maroon, E.
658 A.: Impacts of sea ice mushy thermodynamics in the Antarctic on the coupled Earth
659 system. Geophysical Research Letters, 48, e2021GL094287.
660 https://doi.org/10.1029/2021GL094287, 2021.
661 Fer, I.: Near-inertial mixing in the central Arctic Ocean. J. Phys. Oceanogr., 44, 2031–2049,
662 https://doi.org/10.1175/JPO-D-13-0133.1, 2014.
663 Fetterer, F., Knowles, K., Meier, W. N., Savoie, M., and Windnagel, A. K.: updated daily. Sea
664 Ice Index, Version 3. Boulder, Colorado USA. NSIDC: National Snow and Ice Data
665 Center. https://doi.org/10.7265/N5K072F8, 2017.
666 Freitas, S. R., Grell, G. A., Molod, A., Thompson, M. A., Putman, W. M., Santos e Silva, C.
667 M. and Souza, E. P.: Assessing the Grell–Freitas convection parameterization in the

NASA GEOS modeling system. J. Adv. Model. Earth Syst., 10, 1266–1289, https://doi.org/10.1029/2017MS001251, 2018.

Freitas, S. R., Grell, G. A., and Li, H.: The Grell–Freitas (GF) convection parameterization: recent developments, extensions, and applications, Geosci. Model Dev., 14, 5393–5411, https://doi.org/10.5194/gmd-14-5393-2021, 2021.

Germe, A., Chevallier, M., y Mélia, D. S., Sanchez-Gomez, E., and Cassou, C.: Interannual predictability of Arctic sea ice in a global climate model: Regional contrasts and temporal evolution. Climate Dynamics, 43(9-10), 2519–2538, 2014.

Grell, G. A., and Freitas, S.: A scale and aerosol aware stochastic convective parameterization for weather and air quality modeling. Atmos. Chem. Phys., 14, 5233–5250, https://doi.org/10.5194/acp-14-5233-2014, 2014.

Guemas, V., Blanchard-Wrigglesworth, E., Chevallier, M., Day, J. J., Déqué, M., Doblas-Reyes, F. J., et al.: A review on Arctic sea-ice predictability and prediction on seasonal to decadal time-scales. Quarterly Journal of the Royal Meteorological Society, 142(695), 546–561, 2016.

Haidvogel, D. B., Arango, H., Budgell, W. P., Cornuelle, B. D., Curchitser, E., Di Lorenzo, E., et al.: Ocean forecasting in terrain-following coordinates: Formulation and skill assessment of the Regional Ocean Modeling System, Journal of Computational Physics, 227, 3595–3624, 2008.

Hecht, M. W., Wingate, B. A., and Kassis, P.: A better, more discriminating test problem for ocean tracer transport. Ocean Modell. 2 (1–2), 1–15. https://doi.org/10.1016/S1463-5003(00)00004-4, 2000.

Hersbach, H., Bell, B., Berrisford, P., et al.: The ERA5 global reanalysis. Quarterly Journal of the Royal Meteorological Society, 146, 1999-2049. https://doi.org/10.1002/qj.3803, 2020.

Horvat, C., and Tziperman, E.: A prognostic model of the sea-ice floe size and thickness distribution. Cryosphere 9, 2119–2134, 2015.

695 Horvat, C., Tziperman, E., and Campin, J.-M.: Interaction of sea ice floe size, ocean eddies,
696 and sea ice melting. Geophysical Research Letters, 43, 8083–8090.
697 https://doi.org/10.1002/2016GL069742, 2016.
698 Huang, Y., Chou, G., Xie, Y., & Soulard, N.: Radiative control of the interannual variability
699 of Arctic sea ice. Geophysical Research Letters, 46, 9899– 9908.
700 https://doi.org/10.1029/2019GL084204, 2019.
701 Itoh, M., Nishino, S., Kawaguchi, Y., and Kikuchi, T.: Barrow Canyon volume, heat, and
702 freshwater fluxes revealed by long-term mooring observations between 2000 and 2008.
703 J. Geophys. Res. Oceans, 118, 4363–4379, https://doi.org/10.1002/jgrc.20290, 2013.
704 Jung, T., Gordon, N.D., Bauer, P., Bromwich, D.H., Chevallier, M., Day, J.J., Dawson, J.,
705 Doblas-Reyes, F., Fairall, C., Goessling, H.F., Holland, M., Inoue, J., Iversen, T., Klebe,
706 S., Lemke, P., Losch, M., Makshtas. A., Mills, B., Nurmi, P., Perovich, D., Reid, P.,
707 Renfrew, I.A., Smith, G., Svensson, G., Tolstykh, M., and Yang, Q.: Advancing Polar
708 Prediction Capabilities on Daily to Seasonal Time Scales. Bulletin of the American
709 Meteorological Society. https://doi.org/10.1175/BAMS-D-14-00246.1, 2016.
710 Kaleschke, L., Tian-Kunze, X., Maaß, N., Mäkynen, M., and Drusch, M.: Sea ice thickness
711 retrieval from SMOS brightness temperatures during the Arctic freeze-up period.
712 Geophys. Res. Lett., L05501, https://doi.org/10.1029/2012GL050916, 2012.
713 Kapsch, M., Graversen, R. G., Tjernström, M., and Bintanja, R.: The Effect of Downwelling
714 Longwave and Shortwave Radiation on Arctic Summer Sea Ice. Journal of Climate 29,
715 3, 1143-1159, https://doi.org/10.1175/JCLI-D-15-0238.1, 2016.
716 Kay, J. E., L'Ecuyer, T., Gettelman, A., Stephens, G., and O'Dell, C.: The contribution of cloud
717 and radiation anomalies to the 2007 Arctic sea ice extent minimum, Geophys. Res. Lett.,
718 35, L08503, doi:10.1029/2008GL033451, 2008.
719 Keen, A., Blockley, E., Bailey, D. A., Boldingh Debernard, J., Bushuk, M., Delhaye, S.,
720 Docquier, D., Feltham, D., Massonnet, F., O'Farrell, S., Ponsoni, L., Rodriguez, J. M.,
721 Schroeder, D., Swart, N., Toyoda, T., Tsujino, H., Vancoppenolle, M., and Wyser, K.:

An inter-comparison of the mass budget of the Arctic sea ice in CMIP6 models, The Cryosphere, 15, 951–982, https://doi.org/10.5194/tc-15-951-2021, 2021.

Kirkman, C. H., IV, and Bitz, C. M.: The Effect of the Sea Ice Freshwater Flux on Southern Ocean Temperatures in CCSM3: Deep-Ocean Warming and Delayed Surface Warming. Journal of Climate 24, 9, 2224-2237, https://doi.org/10.1175/2010JCLI3625.1, 2011.

Kwok, R.: Arctic sea ice thickness, volume, and multiyear ice coverage: Losses and coupled variability (1958–2018). Environmental Research Letters, 13(10), 105005, 2018

Laxon, S., Giles, K. A., Ridout, A. L., Wingham, D. J., Willatt, R., Cullen, R., Kwok, R., Schweiger, A., Zhang, J., Haas, C., Hendricks, S., Krishfield, R., Kurtz, N., Farrell, S., and Davidson, M.: CryoSat-2 estimates of Arctic sea ice thickness and volume, Geophys. Res. Lett., 40, https://doi.org/10.1002/grl.50193, 2013.

Lemieux, J. F., Dupont, F., Blain, P., Roy, F., Smith, G. C., and Flato, G. M.: Improving the simulation of landfast ice by combining tensile strength and a parameterization for grounded ridges. J. Geophys. Res. Oceans, 121:7354–7368, http://dx.doi.org/10.1002/2016JC012006, 2016.

Leonard, B., Mokhtari, S.: ULTRA-SHARP Non oscillatory Convection Schemes for High-Speed Steady Multidimensional Flow. Technical Report. NASA, 1990.

Liang, X., and Losch, M.: On the effects of increased vertical mixing on the Arctic Ocean and sea ice. Journal of Geophysical Research: Oceans, 123, 9266– 9282. https://doi.org/10.1029/2018JC014303, 2018.

Liu, J., Song, M., Horton, R., and Hu, Y.: Revisiting the potential of melt pond fraction as a predictor for the seasonal Arctic sea ice minimum. Environmental Research Letters, 10, 054017. https://doi.org/10.1088/1748-9326/10/5/054017, 2015.

Liu, J., Chen, Z., Hu, Y., Zhang, Y., Ding, Y., Cheng, X., et al.: Towards reliable arctic sea ice prediction using multivariate data assimilation. Science Bulletin, 64(1), 63–72, 2019.

747 Merryfield, W., Lee, W.-S., Wang, W., Chen, M., and Kumar, A.: Multi-system seasonal
748 predictions of Arctic sea ice. Geophysical Research Letters, 40, 1551–1556.
749 https://doi.org/10.1002/grl.50317, 2013.
750 Mallett, R. D. C., Stroeve, J. C., Cornish, S. B. Crawford, A. D., Lukovich, J. V., Serreze, M.
751 C., Barrett, A. P., Meier, W. N., Heorton, H. D. B. S., and Tsamados, M.: Record winter
752 winds in 2020/21 drove exceptional Arctic sea ice transport. Commun Earth Environ 2,
753 149, https://doi.org/10.1038/s43247-021-00221-8, 2021.
754 Maslanik, J. and Stroeve, J.: Near-Real-Time DMSP SSMIS Daily Polar Gridded Sea Ice
755 Concentrations, Version 1. Boulder, Colorado USA. NASA National Snow and Ice Data
756 Center Distributed Active Archive Center. https://doi.org/10.5067/U8C09DWVX9LM,
757 1999.
758 McLaughlin, F. A., Carmack, E. C., Williams, W. J., Zimmerman, S., Shimada, K., and Itoh,
759 M.: Joint effects of boundary currents and thermohaline intrusions on the warming of
760 Atlantic water in the Canada Basin, 1993–2007. J. Geophys. Res., 114, C00A12,
761 https://doi.org/10.1029/2008JC005001, 2009.
762 Meehl, G.A., Stocker, T. F., Collins, W. D., et al.: Global Climate Projections. In: Climate
763 Change 2007: The Physical Science Basis. Contribution of Working Group I to the
764 Fourth Assessment Report of the Intergovernmental Panel on Climate Change [Solomon,
765 S., D. Qin, M. Manning, Z. Chen, M. Marquis, K.B. Averyt, M. Tignor and H.L. Miller
766 (eds.)]. Cambridge University Press, Cambridge, United Kingdom and New York, NY,
767 USA, 2007.
768 Msadek, R., Vecchi, G., Winton, M., and Gudgel, R.: Importance of initial conditions in
769 seasonal predictions of Arctic sea ice extent. Geophysical Research Letters, 41, 5208–
770 5215. https://doi.org/10.1002/2014GL060799, 2014.
771 Nakanishi, M., and Niino., H.: Development of an improved turbulence closure model for the
772 atmospheric boundary layer. J. Meteor. Soc. Japan, 87, 895–912,
773 https://doi.org/10.2151/jmsj.87.895, 2009.

774 Naughten, K. A., Galton-Fenzi, B. K., Meissner, K. J., England, M. H., Brassington, G. B.,
775 Colberg, F., Hattermann, T., and Debernard, J. B.: Spurious sea ice formation caused by
776 oscillatory ocean tracer advection schemes. Ocean Model., 116, 108–117, 2017.
777 Naughten, K. A., Meissner, K. J., Galton-Fenzi, B. K., England, M. H., Timmermann, R.,
778 Hellmer, H. H., Hattermann, T., and Debernard, J. B.: Intercomparison of Antarctic ice-
779 shelf, ocean, and sea-ice interactions simulated by MetROMS-iceshelf and FESOM 1.4.
780 Geosci. Model. Dev., 11, 1257–1292, 2018
781 Nerger, L., and Hiller, W.: Software for Ensemble-based Data Assimilation Systems -
782 Implementation Strategies and Scalability. Computers and Geosciences, 55, 110-118.
783 https://doi.org/10.1016/j.cageo.2012.03.026, 2013.
784 Nerger, L., Janjić, T., Schröter, J. and Hiller, W.: A unification of ensemble square root Kalman
785 filters. Monthly Weather Review, 140, 2335-2345. https://doi.org/10.1175/MWR-D-11-
786 00102.1, 2012.
787 Newton, R., Pfirman, S., Schlosser, P., Tremblay, B., Murray, M. and Pomerance, R.: White
788 Arctic vs. Blue Arctic: A case study of diverging stakeholder responses to environmental
789 change. Earth's Future, 4: 396-405. https://doi.org/10.1002/2016EF000356, 2016.
790 Nicolaus M., Katlein, C., Maslanik, J., and Hendricks, S.: Changes in Arctic sea ice result in
791 increasing light transmittance and absorption. Geophysical Research Letters, 39, L24501.
792 https://doi.org/10.1029/2012GL053738, 2012
793 Nicolaus M., and Katlein, C.: Mapping radiation transfer through sea ice using a remotely
794 operated vehicle (ROV). The Cryosphere, 7, 763-77. https://doi.org/10.5194/tc-7-763-
795 2013, 2013.
796 Notz, D., Jahn, A., Holland, M., Hunke, E., Massonnet, F., Stroeve, J., Tremblay, B., and
797 Vancoppenolle, M.: The CMIP6 Sea-Ice Model Intercomparison Project (SIMIP):
798 understanding sea ice through climate-model simulations, Geosci. Model Dev., 9, 3427–
799 3446, https://doi.org/10.5194/gmd-9-3427-2016, 2016.

Ogi, M., Yamazaki, K., and Wallace, J. M.: Influence of winter and summer surface wind anomalies on summer Arctic sea ice extent, Geophys. Res. Lett., 37, L07701, doi:10.1029/2009GL042356, 2010.

Olonscheck, D., Mauritsen, T. and Notz, D.: Arctic sea-ice variability is primarily driven by atmospheric temperature fluctuations. Nat. Geosci. 12, 430–434, https://doi.org/10.1038/s41561-019-0363-1, 2019.

Padman, L., and Dillon, T. M.: Vertical heat fluxes through the Beaufort Sea thermohaline staircase. J. Geophys. Res., 92, 10 799–10 806, https://doi.org/10.1029/JC092iC10p10799, 1987.

Perovich, D., Richter-Menge, J., Jones, K., Light, B., Elder, B., Polashenski, C., Laroche, D., Markus, T., and Lindsay, R.: Arctic sea-ice melt in 2008 and the role of solar heating. Annals of Glaciology, 52(57), 355-359. doi:10.3189/172756411795931714, 2011.

Perovich, D., Richter-Menge, J., Polashenski, C., Elder, B., Arbetter, T., and Brennick, O.: Sea ice mass balance observations from the North Pole Environmental Observatory, Geophys. Res. Lett., 41, 2019– 2025, doi:10.1002/2014GL059356, 2014.

Peterson, K., Arribas, A., Hewitt, H., Keen, A., Lea, D., and McLaren, A.: Assessing the forecast skill of Arctic sea ice extent in the GloSea4 seasonal prediction system. Climate Dynamics, 44(1-2), 147–162, 2015.

Pham, D. T.: Stochastic methods for sequential data assimilation in strongly nonlinear systems. Mon. Wea. Rev., 129, 1194–1207, 2001.

Rasch, P. J.: Conservative shape-preserving two-dimensional transport on a spherical reduced grid, Mon. Wea. Rev, 122, 1337-1350, 1994.

Reynolds, R. W., Smith, T. M., Liu, C., Chelton, D. B., Casey, K. S., and Schlax, M. G.: Daily High-Resolution-Blended Analyses for Sea Surface Temperature, Journal of Climate, 20(22), 5473-5496, 2007.

825 Ricker, R., Hendricks, S., Kaleschke, L., Tian-Kunze, X., King, J., and Haas, C.: A weekly
826 Arctic sea-ice thickness data record from merged CryoSat-2 and SMOS satellite data,
827 The Cryosphere, 11, 1607–1623, https://doi.org/10.5194/tc-11-1607-2017, 2017.
828 Roach, L. A., Bitz, C. M., Horvat, C., and Dean, S. M.: Advances in modeling interactions
829 between sea ice and ocean surface waves. Journal of Advances in Modeling Earth
830 Systems, 11. https://doi.org/10.1029/2019MS001836, 2019.
831 Roach, L. A., Horvat, C., Dean, S. M., and Bitz, C. M.: An emergent sea ice floe size
832 distribution in a global coupled ocean–sea ice model. Journal of Geophysical Research:
833 Oceans, 123(6), 4322–4337. https://doi.org/10.1029/2017JC013692, 2018.
834 Rocheta, E., Evans, J. P., and Sharma, A.: Can Bias Correction of Regional Climate Model
835 Lateral Boundary Conditions Improve Low-Frequency Rainfall Variability?, Journal of
836 Climate, 30(24), 9785-9806, 2017.
837 Rocheta, E., Evans, J. P. and Sharma, A.: Correcting lateral boundary biases in regional climate
838 modelling: the effect of the relaxation zone. Clim. Dyn., 55, 2511–2521.
839 https://doi.org/10.1007/s00382-020-05393-1, 2020.
840 Serreze, M. C. and Meier, W. N.: The Arctic's sea ice cover: trends, variability, predictability,
841 and comparisons to the Antarctic. Ann. N.Y. Acad. Sci., 1436: 36-53.
842 https://doi.org/10.1111/nyas.13856, 2019.
843 Saha, S., Moorthi, S., Wu, X., et al.: The NCEP climate forecast system version 2. J. Clim.
844 27:2185–2208, 2014.
845 Schmidt, G. A., Bitz, C. M., Mikolajewicz, U., and Tremblay, L.-B.: Ice–ocean boundary
846 conditions for coupled models, Ocean Model., 7, 59–74, 2004.
847 Shchepetkin, A.F., McWilliams, J. C.: Quasi-monotone advection schemes based on explicit
848 locally adaptive dissipation. Mon. Weather Rev. 126 (6), 1541–1580, 1998.
849 Shchepetkin, A. F., and McWilliams, J. C.: The Regional Ocean Modeling System: A split-
850 explicit, free-surface, topography following coordinates ocean model, Ocean Modelling,
851 9, 347-404, 2005.

852 Shi, X., Notz, D., Liu, J., Yang, H., and Lohmann, G.: Sensitivity of Northern Hemisphere
853 climate to ice–ocean interface heat flux parameterizations, Geosci. Model Dev., 14,
854 4891–4908, https://doi.org/10.5194/gmd-14-4891-2021, 2021.
855 Sigmond, M., Fyfe, J., Flato, G., Kharin, V., and Merryfield, W.: Seasonal forecast skill of
856 Arctic sea ice area in a dynamical forecast system. Geophysical Research Letters, 40,
857 529–534. https://doi.org/10.1002/grl.50129, 2013.
858 Skamarock, W. C., Klemp, J. B., Dudhia, J., Gill, D. O., Barker, D. M., Wang, W. and Powers,
859 J. G.: A Description of the Advanced Research WRF Version 2. NCAR Technical Note,
860 NCAR/TN-468+STR, 2005.
861 Smolarkiewicz, P. K.: Multidimensional positive definite advection transport algorithm: An
862 overview. Int. J. Numer. Methods Fluids, 50, 1123–1144, 2006.
863 Song, Y. and Haidvogel, D. B.: A semi-implicit ocean circulation model using a generalized
864 topography-following coordinate system. J. Comp. Phys., 115(1), 228-244, 1994.
865 Steele, M.: Sea ice melting and floe geometry in a simple ice-ocean model. Journal of
866 Geophysical Research: Oceans, 97(C11), 17,729–17,738.
867 https://doi.org/10.1029/92JC01755, 1992.
868 Stroeve, J., Blanchard-Wrigglesworth, E., Guemas, V., Howell, S., Massonnet, F., and Tietsche,
869 S.: Improving predictions of Arctic sea ice extent, Eos, 96,
870 https://doi.org/10.1029/2015EO031431, 2015.
871 Stroeve, J., Hamilton, L. C., Bitz, C. M., and Blanchard-Wrigglesworth, E.: Predicting
872 September sea ice: Ensemble skill of the SEARCH Sea Ice Outlook 2008 – 2013,
873 Geophys. Res. Lett., 41, 2411-2418, https://doi.org/10.1002/2014GL059388, 2014.
874 Tian-Kunze, X., Kaleschke, L., Maaß, N., Mäkynen, M., Serra, N., Drusch, M., and Krumpen,
875 T.: SMOS-derived thin sea ice thickness: Algorithm baseline, product specifications and
876 initial verification. Cryosphere, 8, 997-1018, https://doi.org/10.5194/tc-8-997-2014,
877 2014.

878 Tietsche, S., Day, J., Guemas, V., Hurlin, W., Keeley, S., Matei, D., et al.: Seasonal to
879 interannual Arctic sea ice predictability in current global climate models. Geophysical
880 Research Letters, 41, 1035–1043. https://doi.org/10.1002/2013GL058755, 2014.
881 Tsamados, M., Feltham, D. L., and Wilchinsky, A. V.: Impact of a new anisotropic rheology
882 on simulations of Arctic sea ice, J. Geophys. Res. Oceans, 118, 91–107,
883 doi:10.1029/2012JC007990, 2013.
884 Turner, A. K., and Hunke, E. C.: Impacts of a mushy-layer thermodynamic approach in global
885 sea-ice simulations using the CICE sea-ice model, J. Geophys. Res. Oceans, 120, 1253-
886 1275, doi:10.1002/2014JC010358, 2015.
887 Turner, A. K., Hunke, E. C., and Bitz, C. M.: Two modes of sea-ice gravity drainage: A
888 parameterization for large-scale modeling, J. Geophys. Res., 118, 2279–2294,
889 doi:10.1002/jgrc.20171, 2013.
890 Turner, J. S.: Buoyancy Effects in Fluids. Cambridge University Press, 368 pp. 1973.
891 Van den Dool, H.: Empirical Methods in Short-Term Climate Prediction, Oxford Univ. Press,
892 Oxford, U. K., 2006.
893 Wang, W., Chen, M., and Kumar, A.: Seasonal prediction of Arctic sea ice extent from a
894 coupled dynamical forecast system. Monthly Weather Review, 141(4), 1375–1394, 2013.
895 Warner, J. C., Armstrong, B., He, R., and Zambon, J.: Development of a coupled ocean–
896 atmosphere–wave–sediment transport (COAWST) modeling system. Ocean Modell. 35,
897 230–244, 2010.
898 Woodgate, R. A., Aagaard, K., and Weingartner, T. J.: A year in the physical oceanography of
899 the Chukchi Sea: Moored measurements from autumn 1990–1991. Deep-Sea Res. II, 52,
900 3116–3149, https://doi.org/10.1016/j.dsr2.2005.10.016, 2005.
901 Wu, W., Lynch, A. H., and Rivers, A.: Estimating the Uncertainty in a Regional Climate Model
902 Related to Initial and Lateral Boundary Conditions, Journal of Climate, 18(7), 917-933,
903 2005.

Yang, C.-Y., Liu, J., and Xu, S.: Seasonal Arctic sea ice prediction using a newly developed fully coupled regional model with the assimilation of satellite sea ice observations. Journal of Advances in Modeling Earth Systems, 12, e2019MS001938. https://doi.org/10.1029/2019MS001938, 2020.

Zampieri, L., Goessling, H. F., and Jung, T.: Bright prospects for Arctic sea ice prediction on subseasonal time scales. Geophysical Research Letters, 45, 9731– 9738. https://doi.org/10.1029/2018GL079394, 2018.

Zhang, J. and Rothrock, D.: Modeling global sea ice with a thickness and enthalpy distribution model in generalized curvilinear coordinates. Mon. Wea. Rev., 131, 845–861, 2003.

Zhang, J., Lindsay, R., Steele, M., and Schweiger, A.: What drove the dramatic retreat of arctic sea ice during summer 2007?, Geophys. Res. Lett., 35, L11505, doi:10.1029/2008GL034005, 2008.

Zhang, J., Schweiger, A., Steele, M., and Stern, H.: Sea ice floe size distribution in the marginal ice zone: Theory and numerical experiments. Journal of Geophysical Research: Oceans, 120, 3484–3498. https://doi.org/10.1002/2015JC010770, 2015.

Zhang, J., Stern, H., Hwang, B., Schweiger, A., Steele, M., Stark, M., and Graber, H. C.: Modeling the seasonal evolution of the Arctic sea ice floe size distribution. Elementa: Science of the Anthropocene, 4(1), 126. https://doi.org/10.12952/journal.elementa.000126, 2016.

7. Tables

Table 1 The summary of physic parameterizations used in the Y21_CRTL experiment

WRF physics	
Cumulus parameterization	Grell-Freitas (Freitas et al. 2018; improved from Y20)
Microphysics parameterization	Morrison 2-moment (Morrison et al. 2009; same as Y20)
Longwave radiation parameterization	CAM spectral band scheme (Collins et al. 2004; same as Y20)
Shortwave radiation parameterization	CAM spectral band scheme (Collins et al. 2004; same as Y20)
Boundary layer physics	MYNN2 (Nakanishi and Niino, 2006; improved from Y20)
Land surface physics	Unified Noah LSM (Chen and Dudhia, 2001; improved from Y20)
ROMS physics	
Tracer advection scheme	MPDATA (Smolarkiewicz, 2006; same as Y20)
Tracer vertical mixing scheme	GLS (Umlauf and Burchard, 2003; same as Y20)

Bottom drag scheme	Quadratic bottom friction (QDRAG; (same as Y20)
CICE physics	
Ice dynamics	EVP (Hunke and Dukowicz, 1997; improved from Y20)
Ice thermodynamics	Bitz and Lipscomb (1999; same as Y20)
Shortwave albedo	Delta-Eddington (Briegleb and Light, 2007; same as Y20)

926

927

Table 2 The summary of the prediction experiments and details of experiment designs. Note: All experiments use the CFS operational forecasts as initial and boundary conditions; VT: vertical transformation function; VS: vertical stretching function; SH94: stretching function of Song and Haidvogel (1994); S10: stretching function of Shchepetkin (2010).

Experiment	Physics	Assimilation	ROMS vertical coordinate	Simulation period
Y20_MOD	Physics (old version) listed in Table 1	6 localization radii SSMIS SIC Simply-merged CryoSat-2/SMOS SIT	VT 1 VS SH94 h_c 10m	2018.07.01-2018.10.01
Y21_CTRL	Physics (new version) listed in Table 1	6 localization radii SSMIS SIC Simply-merged CryoSat-2/SMOS SIT	VT 1 VS SH94 h_c 10m	2018.07.01-2018.10.01
Y21_VT	Physics (new version) listed in Table 1	6 localization radii SSMIS SIC Simply-merged CryoSat-2/SMOS SIT	VT 2 VS S10 h_c 300m	2018.07.01-2018.10.01
Y21_RP	Advection: U3H/C4V	6 localization radii	VT 2	2018.07.01-

		SSMIS SIC Simply-merged CryoSat-2/SMOS SIT	VS S10 h_c 300m	2018.10.01
Y21_MUSHY	Same physics as Y21_RP CICE: Mushy layer thermodynamics	6 localization radii SSMIS SIC Simply-merged CryoSat-2/SMOS SIT	VT 2 VS S10 h_c 300m	2018.07.01-2018.10.01
Y21_ SIT	Same physics as Y21_RP	6 localization radii SSMIS SIC OI-merged CryoSat-2/SMOS SIT	VT 2 VS S10 h_c 300m	2018.07.01-2018.10.01
Y21_EXT-7	Same physics as Y21_RP	6 localization radii SSMIS SIC OI-merged CryoSat-2/SMOS SIT	VT 2 VS S10 h_c 300m	2018.07.01-2019.01.31

932

933

8. Figures

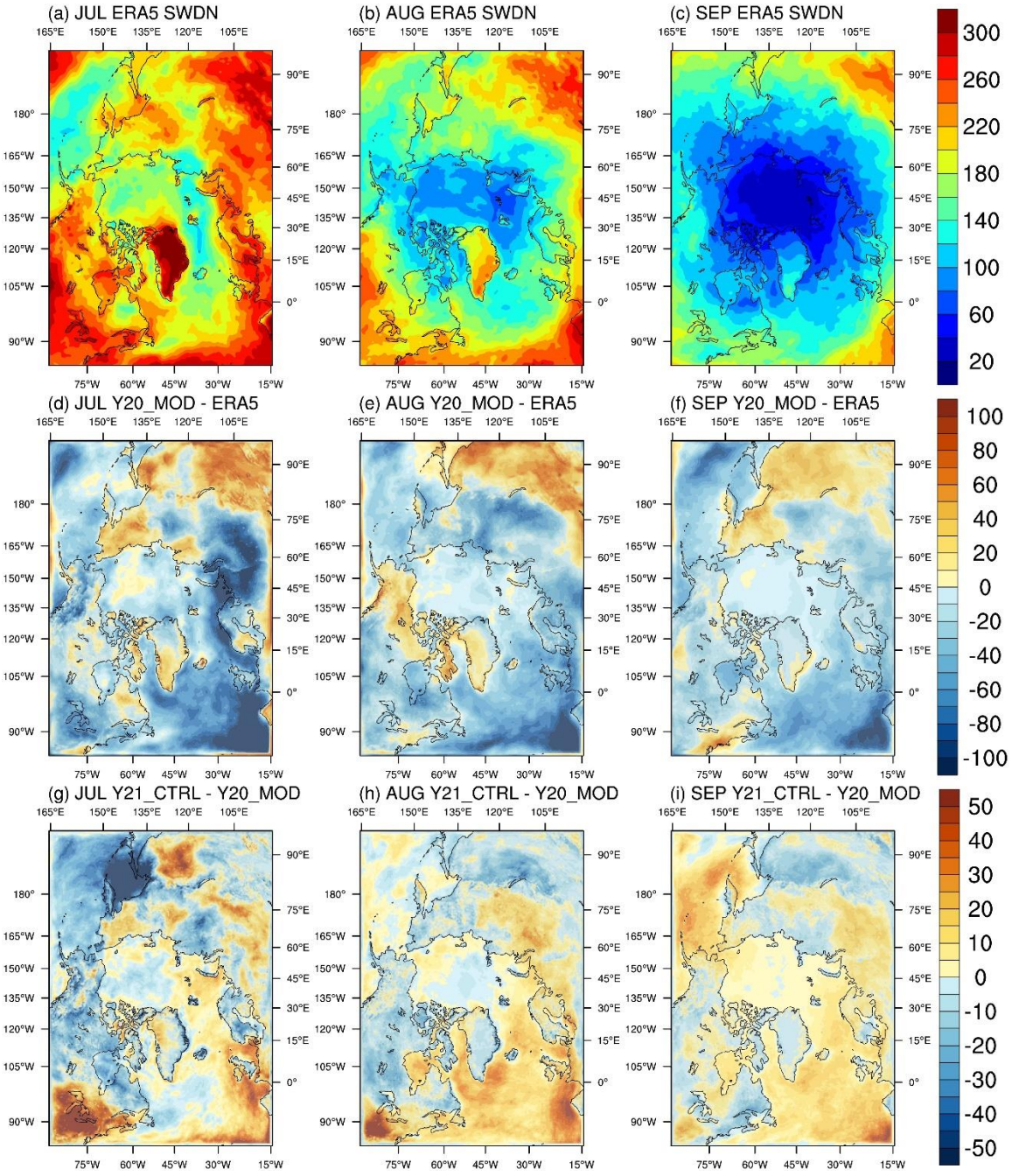

Figure 1 ERA5 monthly mean of downward shortwave radiation at the surface for (a) July, (b) August, and (c) September, the difference between Y20_MOD and ERA5 for (d) July, (e) August, (f) September, and the difference between Y21_CTRL (changes in the atmospheric physics) and Y20_MOD (the original CAPS) for (g) July, (h) August, and (i) September.

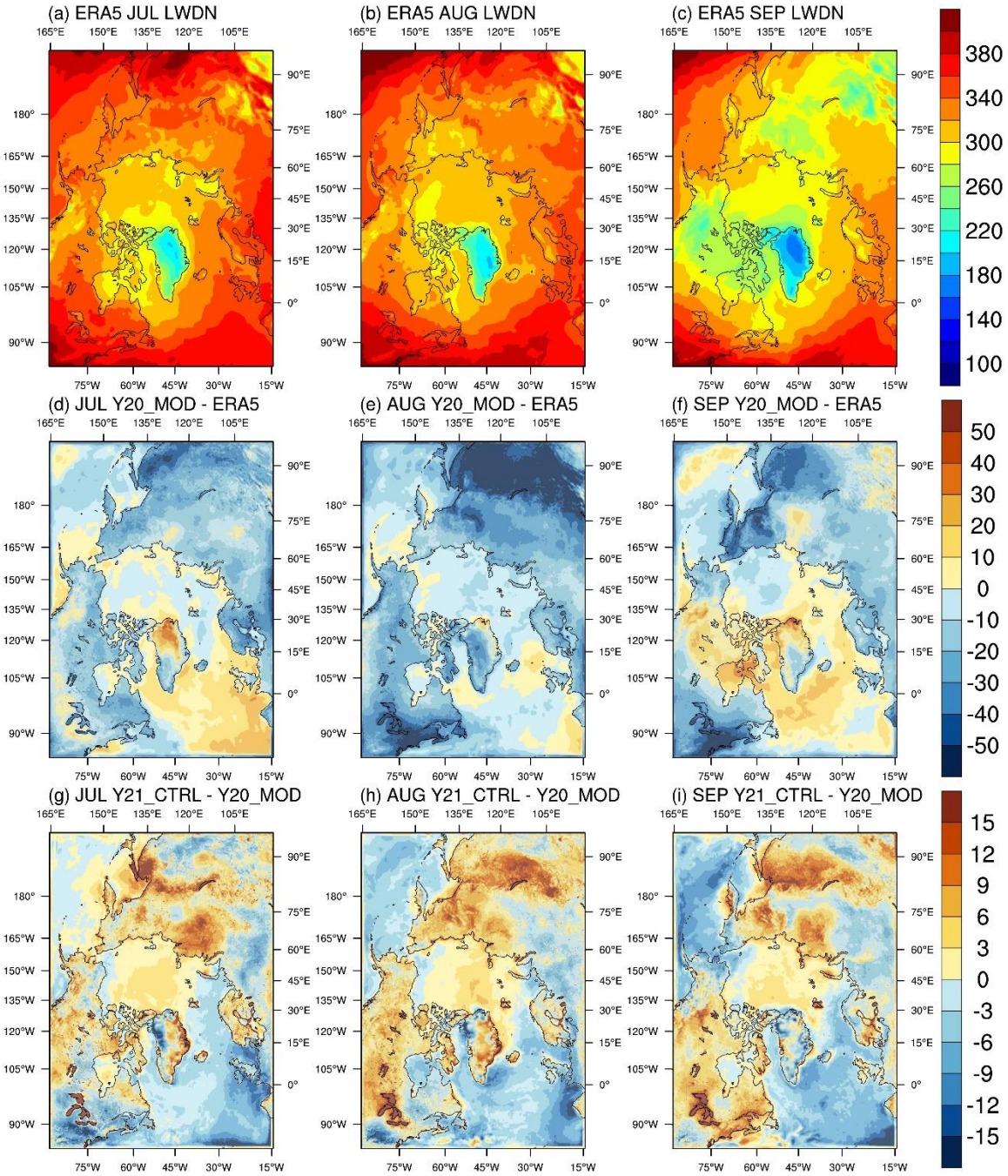

941

942 Figure 2 Same as Figure 1, but for downward thermal radiation at the surface.

943

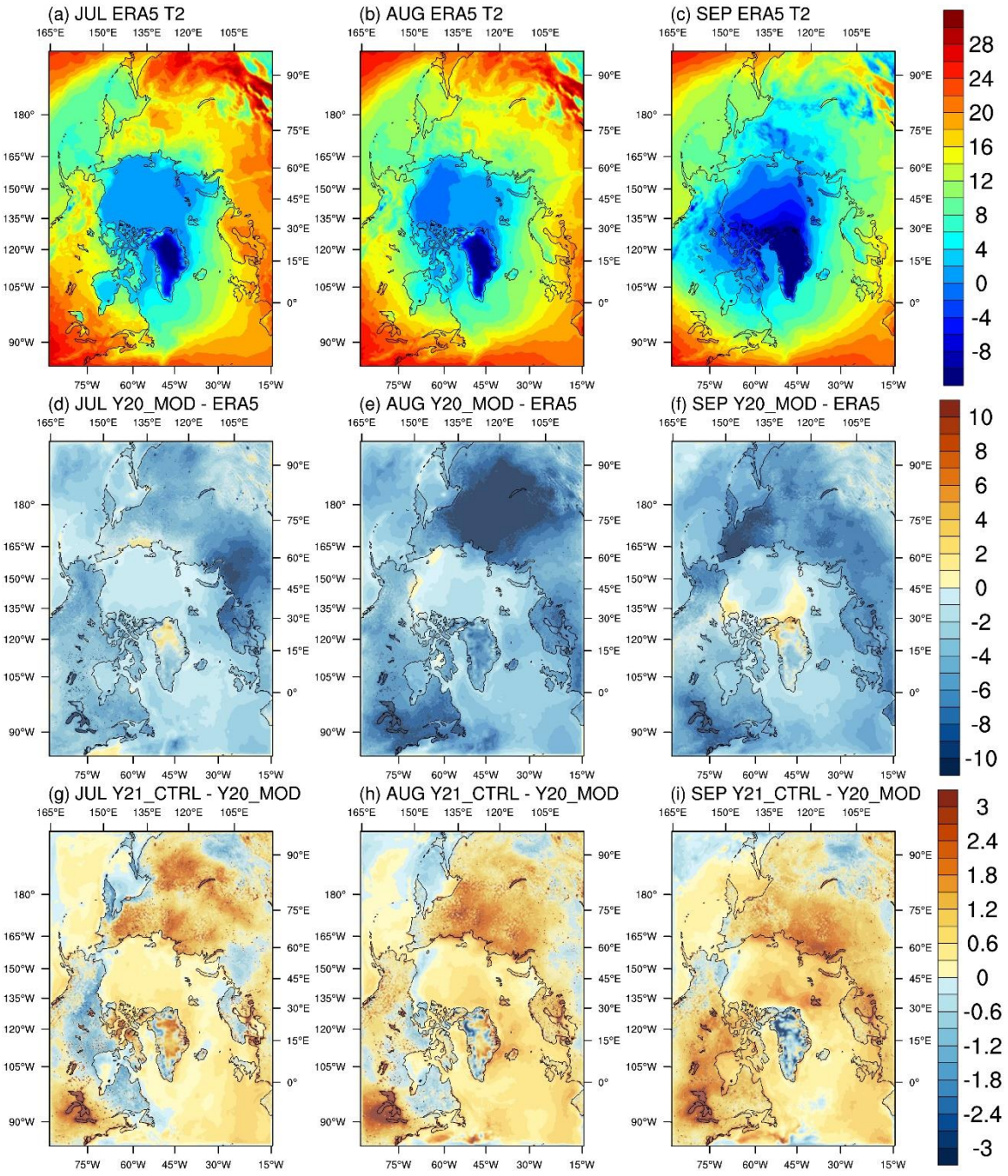

Figure 3 Same as Figure 1, but for near-surface air temperature.

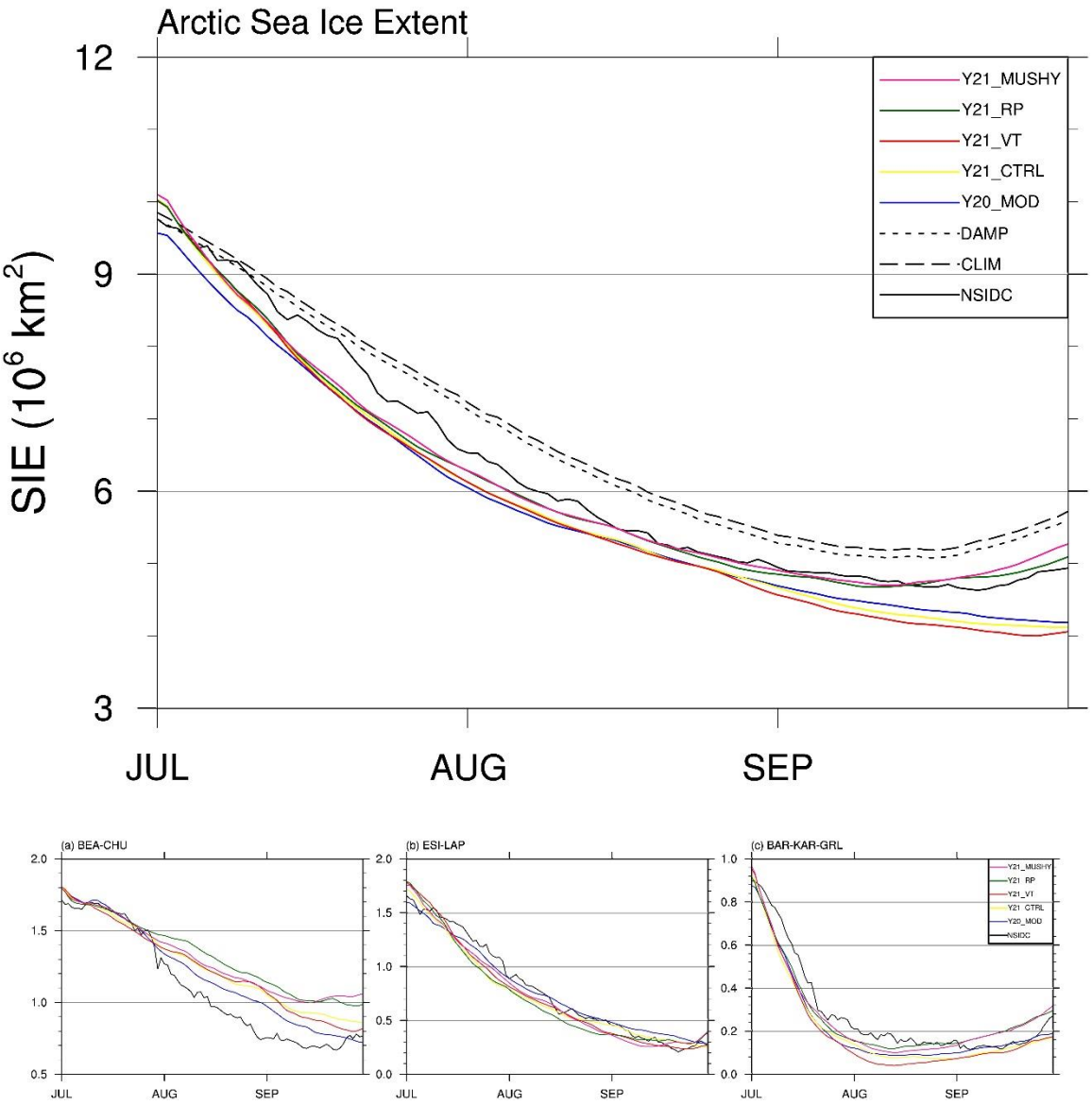

Figure 4 Top panel: Time-series of Arctic sea ice extent for the observations (black line) and the ensemble-mean of Y20_MOD (blue line, the original CAPS), Y21_CTRL (yellow line, changes in the atmospheric physics), Y21_VT (red line, changes in the ocean vertical coordinate), Y21_RP (green line, changes in the oceanic advection), and Y21_MUSHY (pink line, changes in sea ice thermodynamics). Dashed and dotted lines are the climatology and the damped anomaly persistence predictions. Bottom panel: Time-series of the observed (black line) and the ensemble-mean of regional sea ice extents for Y20_MOD (blue line), Y21_CTRL (yellow line), Y21_VT (red line), Y21_RP (green line), and Y21_MUSHY (pink line) for (a) Beaufort-Chukchi Seas, (b) East Siberian-Laptev Seas, and (c) Barents-Kara-Greenland Seas.

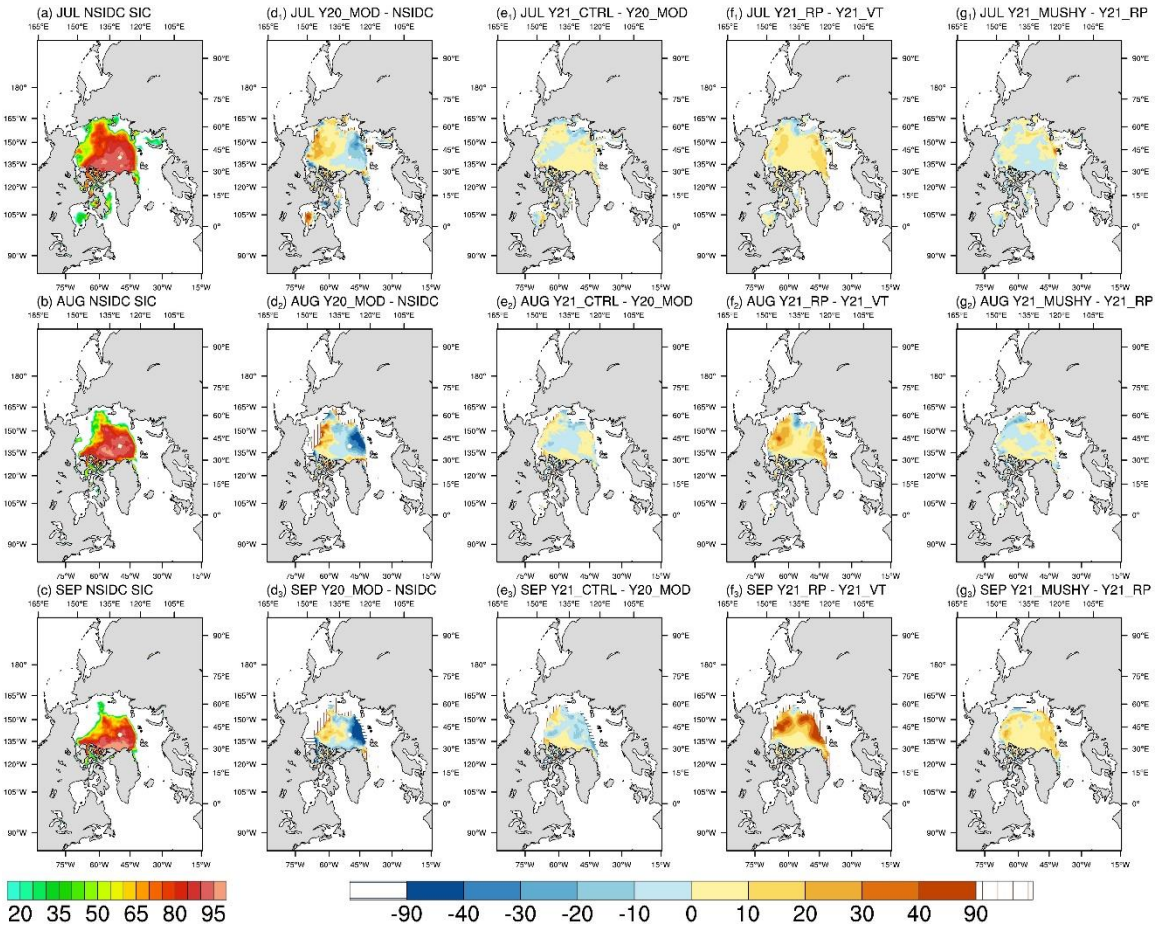

Figure 5 Monthly mean of sea ice concentration for (a) July, (b) August, (c) September of the NSIDC observations, and the difference between the all prediction experiments and the observations for (d_1-g_1) July, (d_2-g_2) August, (d_3-g_3) September. Vertical/horizontal-line areas represent the difference of ice edge location (15% concentration).

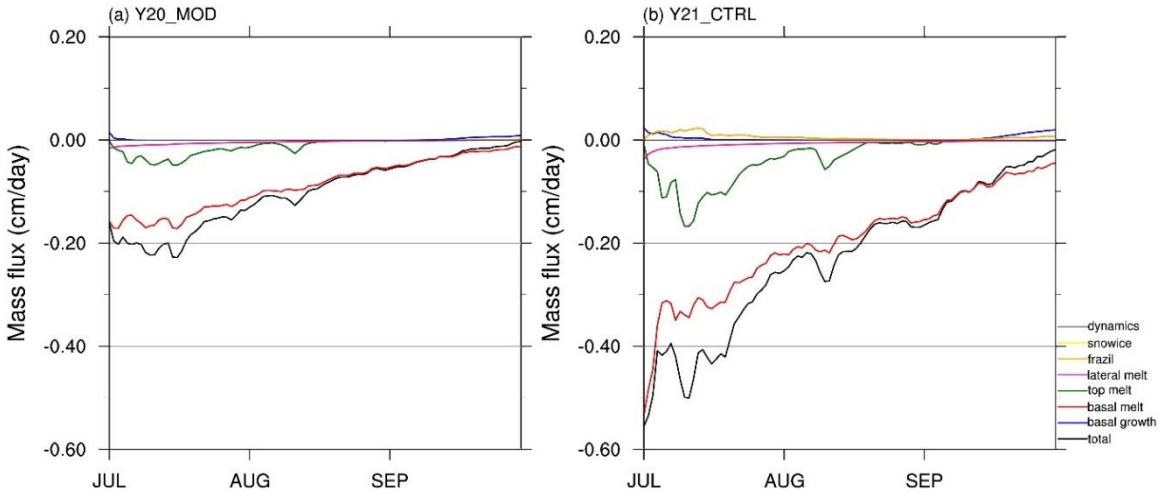

Figure 6 Time-series of sea ice mass budget terms for (a) Y20_MOD (the original CAPS) and (b) Y21_CTRL (changes in the atmospheric physics).

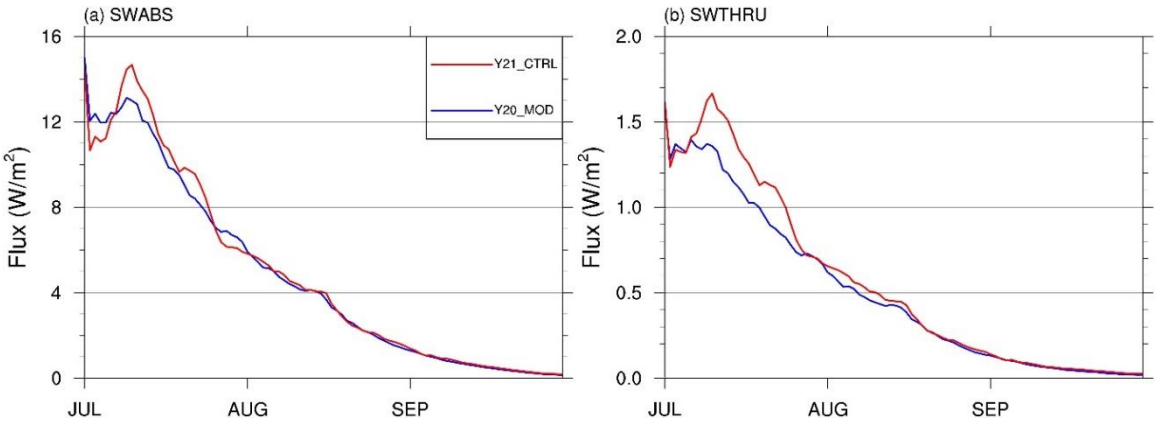

Figure 7 Time-series of (a) shortwave radiation absorbed by ice surface, and (b) penetrating shortwave radiation to the upper ocean averaged over ice-covered grid cells for Y20_MOD (blue line, the original CAPS) and Y21_CTRL (red line, changes in the atmospheric physics).

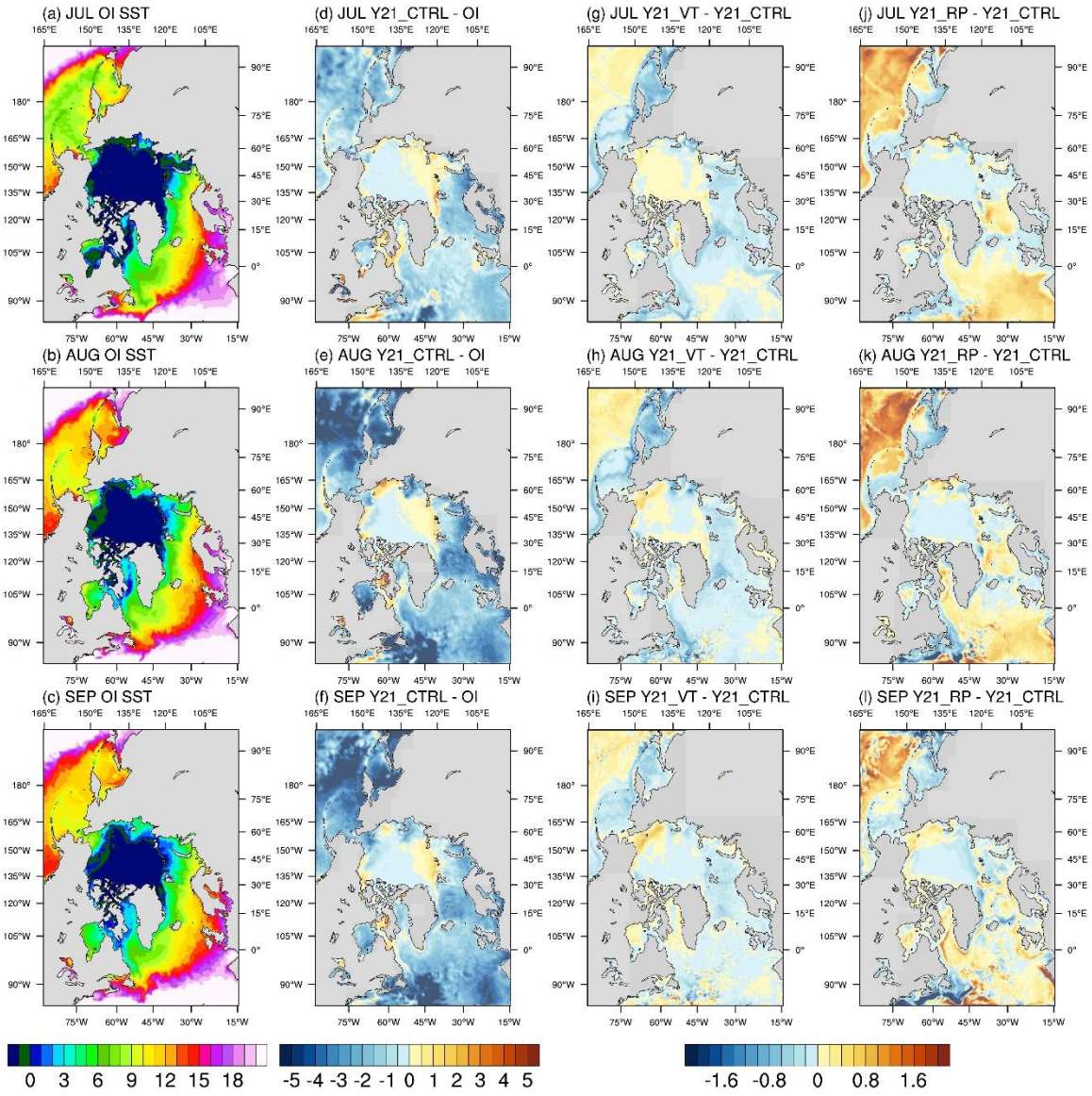

Figure 8 First column: monthly mean of sea surface temperature for (a) July, (b) August, (c) September of the OI SST. Second column: the difference between Y21_CTRL and the OI SST for (d) July, (e) August, (f) September. Right panel: Monthly mean of sea surface temperature difference between Y21_VT/Y21_RP and Y21_CTRL for (g) July, (h) August, (i) September of Y21_VT, (j) July, (k) August, and (l) September of Y21_RP.

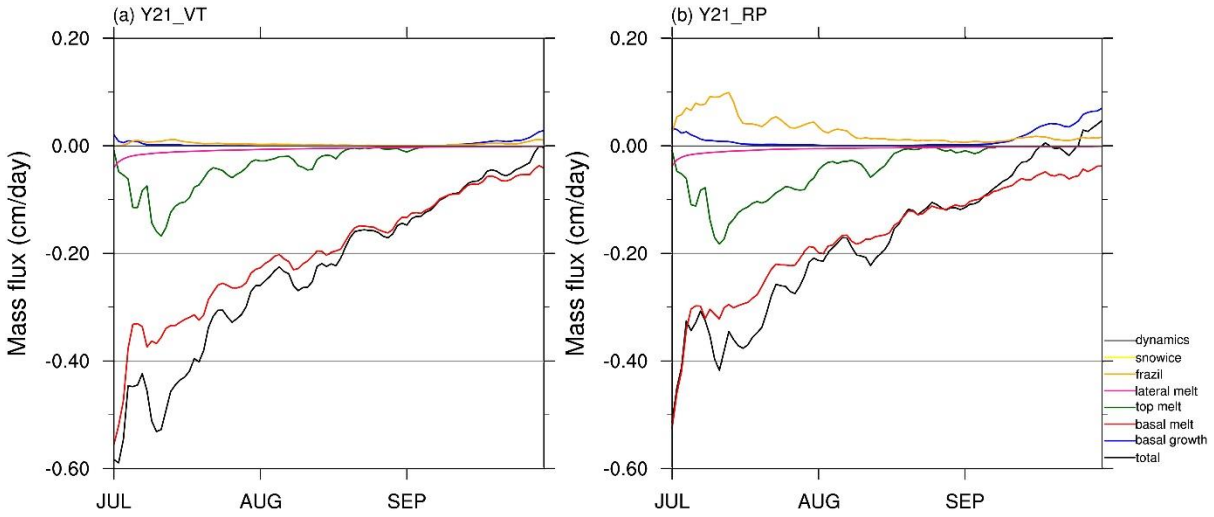

Figure 9 Same as Figure 6, but for (a) Y21_VT (changes in the ocean vertical coordinate), and (b) Y21_RP (changes in the oceanic advection).

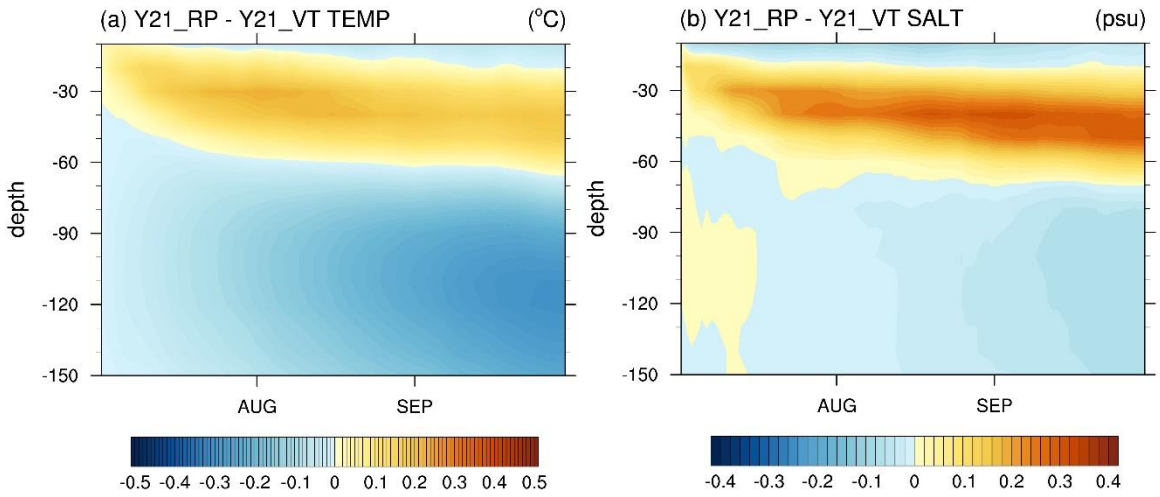

986

987 Figure 10 (a) the average temperature profile of upper 150 m under ice-covered areas for the

988 difference between Y21_RP and Y21_VT. (b) same as (a), but for the salinity profile.

989

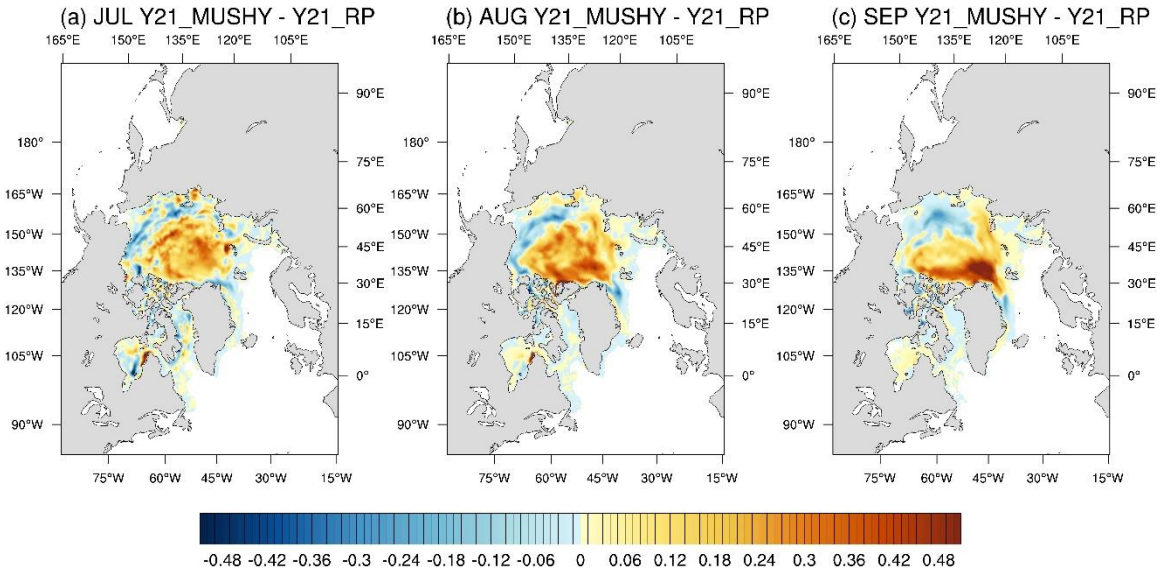

990

991 Figure 11 Monthly mean of sea ice thickness difference between Y21_MUSHY (changes in

992 sea ice thermodynamics) and Y21_RP for (a) July, (b) August, and (c) September.

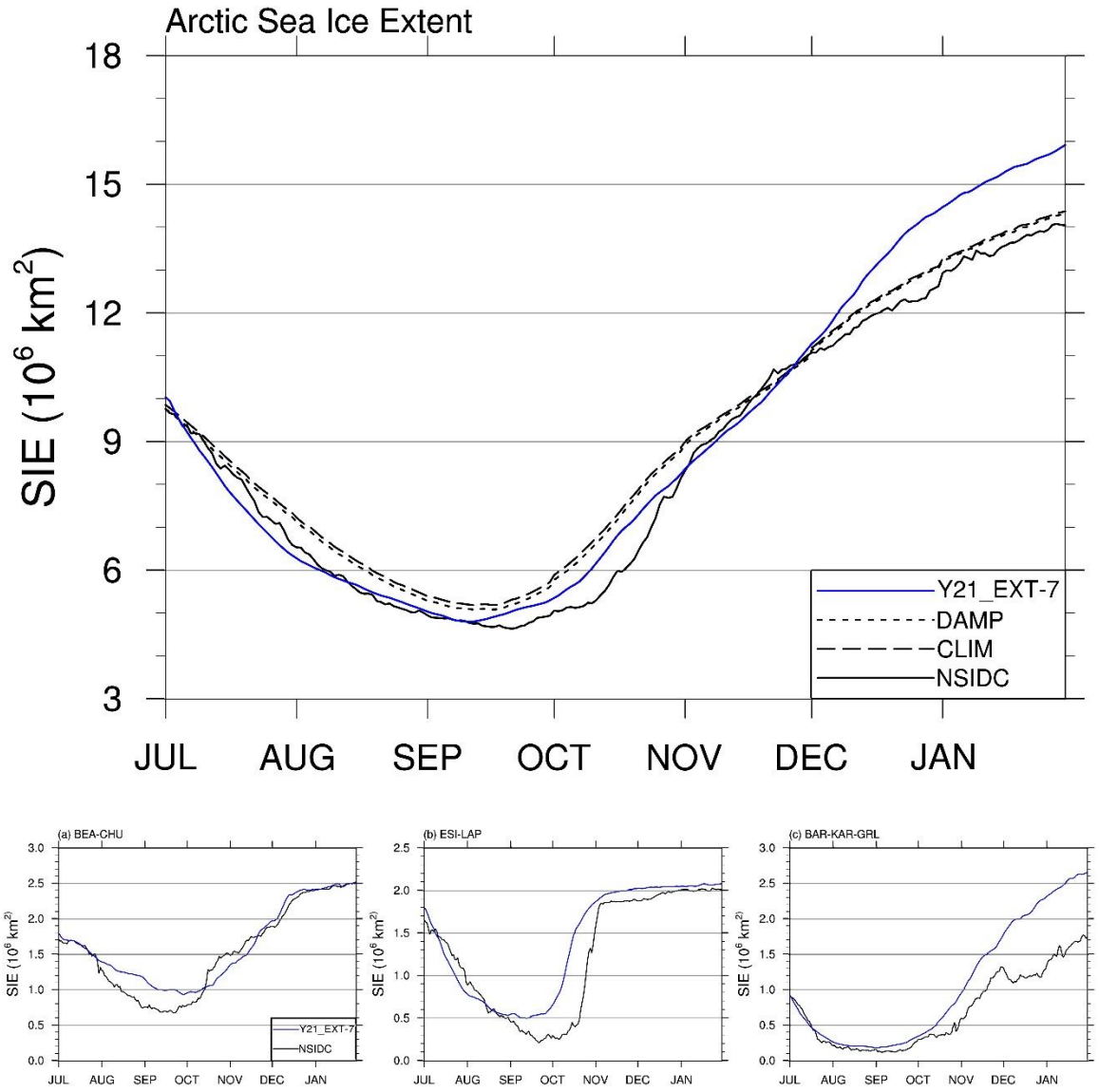

993

994 Figure 12 Same as Figure 4, but for Y21_EXT-7.

995

996